

Proper orthogonal decomposition in Squire's coordinate system for dynamical models of channel turbulence

By VEJAPONG JUTTIJUDATA¹, JOHN L. LUMLEY²
AND DIETMAR REMPFER³

¹Department of Aerospace Engineering, Faculty of Engineering, Kasetsart University,
Jatujak, Bangkok 10900, Thailand

²Sibley School of Mechanical and Aerospace Engineering, Cornell University,
Ithaca, NY 14853, USA

³Department of Materials, Mechanical and Aerospace Engineering, Illinois Institute
of Technology, Chicago, IL 60616, USA

(Received 24 October 2003 and in revised form 1 February 2005)

The convergence rate and the structures of the proper orthogonal decomposition (POD) reconstruction are re-examined. The relatively slow convergence rate of the wall-normal velocity and the over-prediction of the Reynolds shear stress from POD-based representations of near-wall turbulence suggest that coherent structures are too well correlated. This is a consequence of the directional preference of the eigenfunctions toward the most energetic data (the streamwise motion at $x_2^+ = 13$) which may be relaxed by extracting the POD eigenfunctions from the streak modes and the streamwise vortex modes separately. The rate of convergence and representation of structures may be improved by performing the POD in Squire's coordinate system (PODS). The statistical reconstruction of the localized ($x_2^+ \leq 84$) PODS eigenfunctions from the large-eddy simulation (LES) database suggests that the convergence rate of component energy, Reynolds shear stress and the correlation coefficient of streamwise and wall-normal velocity improve significantly. The PODS eigenvalue spectra and the spatial structures of the eigenfunctions indicate the presence of observed streaks, streamwise vortices, and ejection/sweep events.

Dynamical models of the full channel turbulence are constructed by projecting the Navier–Stokes equations onto the PODS eigenfunctions. The unresolved modes are taken into account by closure models adapted from a constant eddy-viscosity model, dynamic Smagorinsky, and dynamic one-coefficient mixed subgrid-scale (SGS) model. Statistical moments obtained from PODS-based simulations are much more accurate than their counterparts from POD-based simulations. This is particularly true for the mean velocity, streamwise turbulent intensity, Reynolds shear stress and the correlation coefficient of streamwise and wall-normal velocity.

1. Introduction

The presence of organized motions or coherent structures in the random-like turbulent boundary layer is now widely accepted. Over the last thirty years, an enormous amount of data has been obtained from both laboratory observation and numerical simulation on the form of these coherent structures. Much of this has been summarized in Robinson (1991). In the wall region, these coherent structures account for over

80 % of the turbulent kinetic energy and consist of alternating low- and high-speed streaks combined with streamwise vortex motions. Kline *et al.* (1967) and Corino & Brodkey (1969) were among the first to observe the recurring sequence of formation and breakdown of these structures known as the *bursting event*. First, the updraught between the vortices strengthens and the vortices move toward each other. The slow-moving fluid that is ejected away from the wall by the vortices induces inflection points in the mean velocity profile in the spanwise and wall-normal directions. As the updraught is strengthening, the wall shear stress, or drag, is approaching its peak value owing to the high-speed fluid being drawn down toward the wall by the downdraught on the opposite side of the vortex. The inflection in the mean velocity profile creates a secondary instability and a burst of Reynolds stress. This instability transfers energy from large-scale motion (coherent motion) to smaller-scale motion (incoherent motion). As a result of the energy transfer, the vortices are weakened and move apart. Last, high-speed fluid comes down from the outer part of the flow and sweeps the wall clean. In the turbulent boundary layer, it is plausible that the dynamics of the coherent structures might be restricted to a very low-dimensional space and be much simpler than that of the full Navier–Stokes equations. In the light of an order-of-magnitude analysis, a better grasp of the dynamics of these coherent structures could be key to a better understanding of the turbulent boundary layer as a whole.

Lumley (1967) proposes an objective technique to extract the coherent structures from a random-like turbulent background. The method consists of extracting candidate structures that are best correlated, in an average sense, to the turbulent velocity field. The coherent structures are described by the orthogonal eigenfunctions of the proper orthogonal decomposition (POD), also known as the Karhunen–Loève decomposition (see Loève 1955; Sirovich 1987; Berkooz, Holmes & Lumley 1993; Holmes, Lumley & Berkooz 1996). The resulting structures are also optimal in the sense that the POD representation converges more rapidly (in an energy mean) than any other linear representation.

In an early use of the POD in boundary layers, Bakewell & Lumley (1967) extract the POD of the wall region from the two-point correlations of a single velocity component based on experimental fully developed pipe flow data. Later Herzog (1986) uses the same facility as Bakewell & Lumley (1967) to perform a fully three-dimensional study of the wall region. Moin & Moser (1989), Sirovich, Ball & Keefe (1990), Ball, Sirovich & Keefe (1991) and Sirovich, Ball & Handler (1991) thoroughly study the coherent structures from the POD based on numerical fully developed channel flow data. These studies lead to the identification of the coherent structures consisting of pairs of counter-rotating streamwise vortices which produce a strong updraught of low-speed fluid away from the wall and a more gentle downdraught of high-speed fluid toward the wall.

The dynamical equations for the coherent structures may be obtained by projecting the Navier–Stokes equations onto the low-order eigenfunctions, describing the most energetic structures. These dynamical equations of the coherent structures are usually referred to as the low-dimensional models. The incoherent motion is taken into account by closure models. In the wall region of turbulent boundary layers, the coherent structures are strong enough that we may be able to confine the models to a very low-dimensional subspace and employ dynamical system tools in order to study the qualitative dynamics of the flows. The ten-dimensional model by Aubry *et al.* (1988) qualitatively reproduces the bursting process of turbulence in the wall region. Aubry *et al.*'s model exhibits intermittent features reminiscent of those found in the wall region of boundary layers.

In spite of the great success of qualitative results from low-dimensional models, their quantitative studies and applications as predictive tools are quite limited. In early investigations of the quantitative accuracy of low-dimensional models, Podvin & Lumley (1998) and Podvin (2001) validate the low-dimensional models of boundary layers (minimal flow unit in Podvin & Lumley (1998) and the near-wall region of Aubry *et al.* (1988) in Podvin (2001)), including the phase-space plots, time series and integrations of DNS and models from the same initial conditions. However, there is no quantitative estimate of the model's predictive accuracy. Gibson (2002) further investigates both short-term and long-term tracking as well as the model statistics for the wall region and Couette flow model. He re-examines the assumptions of the mean velocity model and different boundary conditions for upper surface in Aubry *et al.*'s wall region model (also see the discussion in §4.2) in an effort to improve the quantitative accuracy. He suggests replacing the mean velocity model in the model by the dynamical equation derived directly from the Galerkin projection onto the streamwise- and spanwise-invariant modes. Also he finds that it is necessary to enforce both velocity and the pressure boundary conditions at the upper surface in the model. There are also attempts to use POD-based models as predictive tools. Omurtag & Sirovich (1999) perform a low-dimensional simulation of turbulent channel flow and compare the statistics of mean velocity, turbulent intensities and Reynolds shear stress. Juttijudata, Rempfer & Lumley (2001) develop a new large-eddy simulation (LES) subgrid-stress model (SGS) for the near-wall motion based on the velocity reconstruction of the localized low-dimensional models but could not obtain satisfactory results. The general conclusion from these studies is that the low-dimensional models cannot adequately reproduce the flow with quantitative accuracy unless a large number of modes are used, or better closure models for the unresolved scales can be found.

In our study, we will focus on developing a new set of basis functions for the turbulent boundary layer which will be more suitable for dynamical modelling than the POD basis function set. As mentioned above, one could also try to improve predictive accuracy by developing a more accurate closure model for the unresolved modes. However, the unresolved modes generally contribute to only a fraction of 10 % of the total kinetic energy which is relatively small compared to the energy in the resolved modes. Under this circumstance, the development of an alternative basis might be a more promising way to improve the accuracy of the dynamical models. The issue of the boundary conditions of the localized low-dimensional models and the well-posedness of the problem has been explored in some depth in Gibson (2002) and will not be considered here. Therefore we will only examine the dynamical models of the full channel domain. In order to arrive at quantitatively accurate models, we will only focus on very large systems of equations, which are in the neighbourhood of 3000–6000 coupled complex ordinary differential equations. The number of equations in the systems is only smaller than the LES we use by a factor of about 30. It is impossible to draw any analytical understanding or study the bifurcation from such huge systems but they are not the goal of this study. Compared to Aubry *et al.*'s ten-dimensional model, our dynamical models are in no way to be claimed as low-dimensional models. Nevertheless, the heart of our dynamical models lies in the projection of the Navier–Stokes equations onto the POD-type basis functions, just like low-dimensional models, and may be (misleadingly) referred to low-dimensional models from time to time.

This paper is organized as follows: §2 examines the convergence rate, the velocity structures and shortcomings of the (localized) POD reconstruction. The concept of

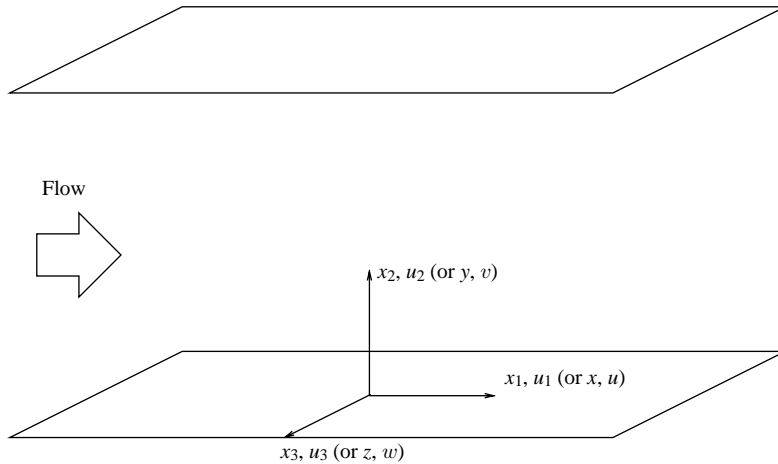


FIGURE 1. Coordinate system in channel.

the POD in Squire's coordinate system (PODS) is explored in § 3. Section 4 derives the dynamical models of the PODS and the LES SGS models are modified to account for the unresolved motion. Section 5 summarizes the numerical methods to solve our dynamical models and the parameters of different simulations. Section 6 presents results from different dynamical model simulations. We conclude our study in § 7.

2. Proper orthogonal decomposition of channel turbulence in a physical coordinate system

2.1. Channel turbulence

In the channel, the domain, Ω , is bounded by two separated walls located at $x_2 = \pm 1$ (normalized by channel half-width, δ) in the wall-normal direction. Its size in the streamwise and spanwise directions is L_1 and L_3 respectively. We shall assume periodicity in the streamwise and spanwise directions and refer to these directions as homogeneous. Throughout we use the Cartesian coordinate system shown in figure 1 in which (x_1, x_2, x_3) and (x, y, z) denote the streamwise, wall-normal, and spanwise direction respectively. Velocity components in these directions are denoted by (u_1, u_2, u_3) and (u, v, w) . Note that the Navier–Stokes equations and boundary condition for channel turbulence are invariant under certain symmetries:

(a) spanwise reflection around the mid-plane of the channel:

$$R_{x_2} : (x_1, x_2, x_3, u_1, u_2, u_3) \longrightarrow (x_1, -x_2, x_3, u_1, -u_2, u_3);$$

(b) wall-normal reflection around the horizontal centreplane of the channel:

$$R_{x_3} : (x_1, x_2, x_3, u_1, u_2, u_3) \longrightarrow (x_1, x_2, -x_3, u_1, u_2, -u_3);$$

(c) streamwise and spanwise translations:

$$T_{\Delta x_1, \Delta x_3} : (x_1, x_2, x_3, u_1, u_2, u_3) \longrightarrow (x_1 + \Delta x_1, x_2, x_3 + \Delta x_1, u_1, u_2, u_3).$$

In other words, the action of these symmetry groups on the velocity ensemble of a channel Navier–Stokes solution results in a velocity ensemble that is also the solution of the equations and boundary condition. In the POD calculation, we also force the wall-normal and spanwise reflection symmetry in the velocity ensemble to improve

the convergence rate of the statistics and to ensure the wall-normal and spanwise reflection symmetry in the resulting eigenfunctions. We also use the streamwise and spanwise translation symmetries to reduce the POD in the streamwise and spanwise directions to Fourier modes (see Holmes *et al.* 1996).

The channel turbulence database in this study is generated by large-eddy simulation (LES) using a dynamic one-coefficient mixed subgrid-scale (SGS) model (see Sarghini, Piomelli & Balaras 1999). The fourth-order wall-normal velocity/vorticity formulation of the Navier–Stokes equations is integrated in time using a Fourier–Chebyshev pseudo-spectral scheme (similar to that in Kim, Moin & Moser 1987). The nonlinear term in the Navier–Stokes equations is cast in the skew-symmetric form and computed without dealiasing. The time-advancement is performed by a semi-implicit third-order Runge–Kutta time-stepping algorithm as in Spalart, Moser & Roger (1991). We maintain a fixed volume flow rate throughout the simulation. The Reynolds number of the channel flow simulation is 4000 based on the laminar centreline velocity, U_c , and half-channel width, δ , equivalent to 172 based on *computed* friction velocity, u_τ (the correlation by Dean (1978) gives $Re_\tau = 174$). Wall units are based on computed friction velocity and viscosity, and denoted by superscript $+$. The computational domain normalized by the half-channel width is $(L_1, L_2, L_3) = (3\pi, 2, \pi)$, equivalent to $(L_1^+, L_2^+, L_3^+) = (1640, 348, 547)$, and the resolution in the simulation is $(N_1, N_2, N_3) = (32, 65, 48)$, equivalent to $(\Delta x_1^+, \Delta x_{2_{min}}^+, \Delta x_3^+) \approx (51, 0.2, 11)$. We apply reflection symmetries to 600 independent realizations (separated in time by approximately $\Delta t = 1.5\delta/U_c$) in the statistical calculation. The symmetries produce a total of $4 \times 600 = 2400$ realizations in the ensemble. For one-point statistics, the number of samples is increased by averaging over horizontal (homogeneous) planes. Only the *filtered* part of the LES velocity field is accounted for in the one-point turbulence statistics and two-point spectral-density tensor unless stated otherwise.

2.2. The POD

The reader is directed to a monograph by Holmes *et al.* (1996) and review articles by Berkooz *et al.* (1993) and Sirovich (1987) for a comprehensive review of the POD. The fundamental idea of the POD is to look for the single, deterministic function that is most similar (in an average sense) to the members of $u_i(\mathbf{x})$ within an ensemble of realizations. The optimality constraint reduces to an eigenvalue problem whose kernel is the two-point spectral-density tensor:

$$\int_{\Omega_2} \langle \hat{u}_{i_k}(x_2) \hat{u}_{j_k}^*(x'_2) \rangle \phi_{j_k}(x'_2) dx'_2 = \lambda_k \phi_{i_k}(x_2), \quad (2.1)$$

where $\hat{u}_{i_k}(x_2)$ is the Fourier-transformed fluctuating velocity defined by

$$\hat{u}_{i_k} = \frac{1}{L_1 L_3} \int_0^{L_1} \int_0^{L_3} u_i(x_1, x_2, x_3) e^{-i(k_1 x_1 + k_3 x_3)} dx_3 dx_1,$$

and the corresponding velocity is given by

$$u_i(x_1, x_2, x_3) = \sum_{k=-\infty}^{\infty} \hat{u}_{i_k} e^{i(k_1 x_1 + k_3 x_3)}.$$

The asterisk denotes the complex conjugate and $\mathbf{k} = (k_1, k_3)$ is the wavenumber-vector. In general, the averaging operation may either be an ensemble or temporal or spatial or phase average. The eigenfunctions and eigenvalues of (2.1) are sometimes referred to as the *empirical* eigenfunctions and eigenvalues. We implicitly use the

fact that the eigenfunctions in homogeneous directions (streamwise and spanwise) reduce to Fourier modes. Each realization may be decomposed into a mixed discrete Fourier–POD decomposition of the form

$$u_i(\mathbf{x}, t) = \sum_{k=-\infty}^{\infty} \sum_{n=1}^{\infty} a_k^{(n)}(t) e^{i(k_1 x_1 + k_3 x_3)} \phi_{i_k}^{(n)}(x_2). \quad (2.2)$$

From (2.2), the Fourier-transformed velocity is given by

$$\hat{u}_{i_k}(x_2) = \sum_{n=1}^{\infty} a_k^{(n)} \phi_{i_k}^{(n)}(x_2), \quad (2.3)$$

in which the modal coefficients can be computed from the inner product of the velocity vector and the eigenfunctions,

$$a_k^{(n)} = (\hat{u}_{i_k}, \phi_{i_k}^{(n)}), \quad (2.4)$$

where the inner product is defined by

$$(\hat{u}_{i_k}, \phi_{i_k}^{(n)}) = \int_{\Omega_2} (\hat{u}_{1_k} \phi_{1_k}^{(n)*} + \hat{u}_{2_k} \phi_{2_k}^{(n)*} + \hat{u}_{3_k} \phi_{3_k}^{(n)*}) dx_2. \quad (2.5)$$

We normalize the eigenfunctions such that

$$(\phi_{i_k}^{(n)}, \phi_{i_k}^{(p)}) = \delta_{np}.$$

From Hilbert–Schmidt theory we know that there is a denumerable infinity of the eigenvalues and eigenfunctions that provide a diagonal decomposition of the two-point spectral-density tensor,

$$\langle \hat{u}_{i_k}(x_2) \hat{u}_{j_k}^*(x'_2) \rangle = \sum_{n=1}^{\infty} \lambda_k^{(n)} \phi_{i_k}^{(n)}(x_2) \phi_{j_k}^{(n)*}(x'_2). \quad (2.6)$$

The diagonal decomposition implies that the (random) modal coefficients of the decomposition are uncorrelated on average,

$$\langle a_k^{(n)} a_k^{(m)*} \rangle = \lambda_k^{(n)} \delta_{nm}.$$

We may order $\lambda_k^{(n)}$ such that $\lambda_k^{(n)} \geq \lambda_k^{(n+1)}$; hence the lowest-order eigenmode corresponds to the most energetic turbulent structures.

Apart from the wall-normal and spanwise reflection symmetries in the velocity ensemble as discussed in §2.1, the incompressibility and no-slip boundary conditions (or any linear boundary condition) are also inherited in the eigenfunctions. These two properties are desirable properties of the basis functions that significantly simplify the dynamical model construction.

2.3. The deficiencies of POD

Although the optimality constraint guarantees the optimality of the eigenfunctions in an energy sense, it does not guarantee the optimality of individual component energy nor Reynolds shear stress. Figures 2(a), 2(b), 2(c) and 2(d) show the statistical reconstruction of streamwise and wall-normal turbulent intensity, Reynolds shear stress and the correlation coefficient of the streamwise and wall-normal velocity from the localized POD eigenfunctions in the region $0 \leq x_2^+ \leq 84$ compared to the statistics from the LES *filtered* velocity field. To solve the eigenvalue problem, we expand the two-point spectral-density tensor using Chebyshev polynomials in the wall-normal

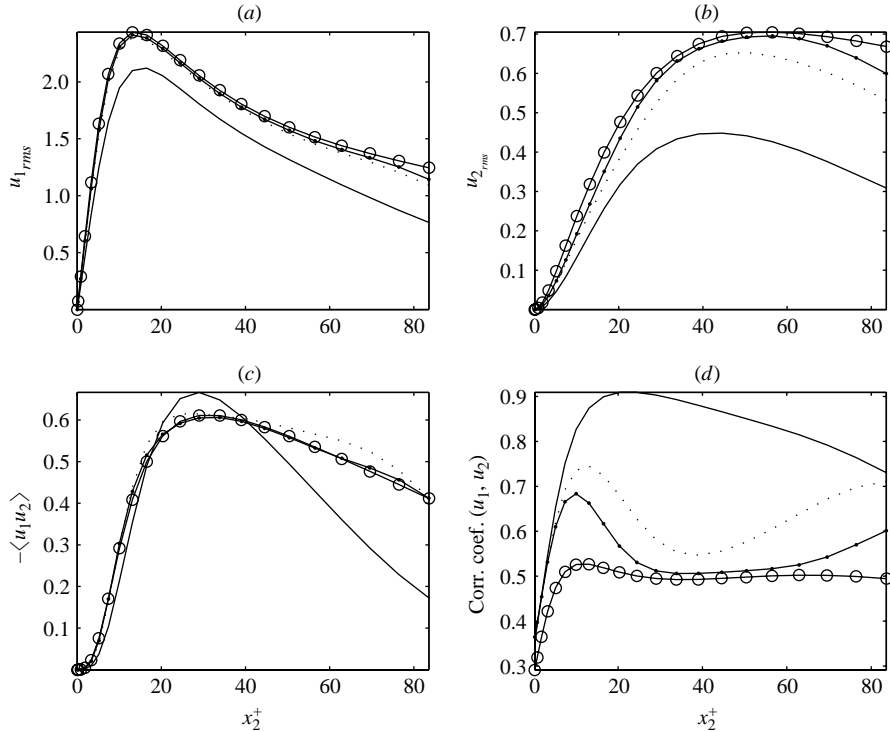


FIGURE 2. Statistical reconstruction from the localized ($0 \leq x_2^+ \leq 84$) POD eigenfunctions: (a) streamwise turbulent intensity, (b) wall-normal turbulent intensity, (c) Reynolds shear stress and (d) correlation coefficient of streamwise and wall-normal velocity: solid, $N = 1$; dotted, $N = 4$; points, $N = 6$; circles, LES.

direction and extract the eigenfunctions in Chebyshev space using a double-precision complex Hermitian eigenvalue solver routine (ZHEEV) in LAPACK. In order to obtain the localized POD eigenfunctions, the integral in (2.1) is evaluated over the portion of the channel with $0 \leq x_2^+ \leq 84$ despite the global Chebyshev representation in the full channel. The resulting eigenfunction Chebyshev coefficients are projected onto the Chebyshev collocation points in the subdomain, $x_2^j/\delta = \cos(\pi/64 \times (j - 1))$ where $j = 44, \dots, 65$. Numerical integration in the inner product is defined by using the trapezoidal rule. Note that in our terminology, speaking of POD velocity reconstruction of the first N families of eigenfunctions implies summation over *all* the Fourier modes; thus, by ‘families of eigenfunctions’ we refer to the set of functions $\phi_{ik}^{(n)}$ with upper index n , for any k .

It is clear that the low-order eigenfunctions contain over 100 % of the Reynolds shear stress as shown in figure 2(c) (see also Moin & Moser 1989). The negative contribution of the Reynolds shear stress in the higher-order eigenfunctions must be included in the velocity expansion in order to remove the overproduction of Reynolds shear stress. Another less obvious deficiency of POD eigenfunctions is the non-uniform convergence rate of individual component energy. One can see in figures 2(a) and 2(b) that the convergence rate of streamwise turbulent intensity is much faster than that of wall-normal turbulent intensity (and the spanwise turbulent intensity shown in Juttijudata (2003)). The overproduction of Reynolds shear stress as shown in figure 2(c) and the relatively slow convergence rate of wall-normal turbulent intensity

result in the overproduction of the correlation coefficient as evident in figure 2(d). Physically, the overproduction of the correlation coefficient implies that the POD eigenfunctions produce structures which are ‘too coherent’. In other words, for a given mean shear rate, the POD eigenfunctions require less input wall-normal turbulent intensity than the physical structures in order to generate the same streamwise turbulent intensity.

A closer examination of the POD eigenvalue problem reveals that the cause of the too-coherent structures is the directional preference of the eigenfunctions (the principal axes of the cloud of data points $\{u_i(\mathbf{x}, t_k)\}$) to the most energetic component, which is the streamwise motion at the location of maximum streamwise component energy ($x_2^+ = 13$), in this case. Because the low-order eigenfunctions prefer the streamwise motion over the wall-normal (and spanwise) motion, the low-order POD representation is likely to almost fully reproduce streamwise turbulent intensity from a given smaller wall-normal turbulent intensity.

The directional preference of the POD may be relaxed by either isolating the more energetic streamwise motion from the less energetic lateral motion or by re-scaling every component to the same order of magnitude. However, the incompressibility condition of the eigenfunctions should be preserved in order to eliminate the pressure contribution from dynamical models; hence the choice of isolating the streamwise component from the lateral components is preferred.

3. Proper orthogonal decomposition of channel turbulence in Squire’s coordinate system

3.1. The PODS

In an early attempt to decouple streamwise modes from lateral modes, Berkooz, Holmes & Lumley (1991) take advantage of the streamwise-invariant assumption in their model. They set the streamwise component of the eigenfunctions as the streamwise mode eigenfunctions, $(\phi_{1(0,k_3)}^{(n)}, 0, 0)$, and the wall-normal and spanwise components of the eigenfunctions as lateral mode eigenfunctions, $(0, \phi_{2(0,k_3)}^{(n)}, \phi_{3(0,k_3)}^{(n)})$, and develop separate low-dimensional models for streamwise and lateral modes. For general non-zero Fourier wavenumber cases, Waleffe (1995) proposes splitting the vector-value basis functions into two orthogonal parts, i.e. $\phi_{ik}^{(n)} = \phi_{ik,S}^{(n)} + \phi_{ik,R}^{(n)}$ where $\phi_{ik,S}^{(n)} = P_{ij}\phi_{jk}^{(n)}$ and $\phi_{ik,R}^{(n)} = (\delta_{ij} - P_{ij})\phi_{jk}^{(n)}$ with the projection matrix $P_{ij} = p_i p_j / (p_k p_k)$ and $p_i = (-k_3, 0, k_1)$. For streamwise-invariant modes, Waleffe’s splitting reduces to Berkooz *et al.*’s splitting. Indeed, Waleffe’s splitting of the eigenfunctions bears some relation to Squire’s transformation (see Squire 1933; Stuart 1963) and the POD in Squire’s coordinate system (PODS), which will be further discussed again at the end of this section.

As suggested in Leonard & Wray (1982) and Moser, Moin & Leonard (1983), it is natural to decompose the velocity vector in Fourier space into ‘plus-modes’ and ‘minus-modes’,

$$U_k^+ = (\hat{u}_k^\parallel, \hat{v}_k, 0), \quad \text{and} \quad U_k^- = (0, 0, \hat{u}_k^\perp),$$

where \hat{u}_k^\parallel and \hat{u}_k^\perp are horizontal velocity components parallel and perpendicular to the wavenumber-vector, defined by

$$\hat{u}_k^\parallel = \frac{k_x \hat{u} + k_z \hat{w}}{|\mathbf{k}|}, \quad (3.1)$$

$$\hat{u}_k^\perp = \frac{-k_z \hat{u} + k_x \hat{w}}{|\mathbf{k}|}, \quad (3.2)$$

where $|\mathbf{k}| = \sqrt{(k_x^2 + k_z^2)}$. The horizontal velocity in the physical coordinate system may be obtained from

$$\hat{u}_{\mathbf{k}} = \frac{k_x \hat{u}^{\parallel} - k_z \hat{u}^{\perp}}{|\mathbf{k}|}, \quad (3.3)$$

$$\hat{w}_{\mathbf{k}} = \frac{k_z \hat{u}^{\parallel} + k_x \hat{u}^{\perp}}{|\mathbf{k}|}. \quad (3.4)$$

We exclude the $\mathbf{k} = (0, 0)$ mode from the representation. This decomposition amounts to Squire's transformation and its corresponding coordinate system is Squire's coordinate system. Note that the orientation of Squire's coordinate system relative to the physical coordinate system changes as a function of the wavenumber-vector.

The incompressibility condition in Squire's coordinate system acts only on the plus-modes:

$$i|\mathbf{k}|\hat{u}_{\mathbf{k}}^{\parallel} + \frac{\partial \hat{v}_{\mathbf{k}}}{\partial y} = 0. \quad (3.5)$$

While the plus-modes need to satisfy both the boundary condition and incompressibility condition, minus-modes need to satisfy only the boundary condition.

In streamwise-invariant space, the plus- and minus-mode Fourier-transformed velocity exactly reduces to the lateral and streamwise modes respectively. On the other hand, in the spanwise-invariant space, the plus- and minus-mode Fourier-transformed velocity reduces to the streamwise and wall-normal modes and spanwise modes. Clearly we will benefit from Squire's transformation only if the most energetic structures are approximately streamwise-invariant. In that case Squire's transformation allows us to approximately isolate streamwise motion in minus-modes (that need to satisfy only the boundary condition) from lateral motion in plus-modes (that need to satisfy both divergence-free and boundary conditions). The transformation to Squire's coordinate system gives us the freedom to solve the POD eigenvalue problem in plus- and minus-modes independently and still produces divergence-free basis functions. Flow visualization suggests the observed streaks in turbulent boundary layers (the most energetic structures) are relatively elongated in the streamwise direction: the streamwise length often exceeds $1500 \nu/u_{\tau}$, and the spanwise width ranges from 20 to $80 \nu/u_{\tau}$, e.g. Robinson (1991). In addition, the peaks of the one-dimensional streamwise-component energy spectra at $x_2^+ = 13$ are concentrated in the zero-streamwise-wavenumber subspace. Under this condition, a substantial fraction of the streamwise component energy is confined to the neighbourhood of the streamwise-invariant modes and the usage of Squire's transformation is advantageous.

Let us now derive the formulation of the POD in Squire's coordinate system (PODS). The basic idea is to separately apply the POD formulation to the plus- and minus-modes for each Fourier mode. The PODS eigenvalue problems are

$$\int_{\Omega_2} \langle \hat{U}_{i\mathbf{k}}^+(x_2) \hat{U}_{j\mathbf{k}}^{+*}(x'_2) \rangle \phi_{j\mathbf{k}}^+(x'_2) dx'_2 = \lambda_{\mathbf{k}}^+ \phi_{i\mathbf{k}}^+(x_2), \quad (3.6)$$

$$\int_{\Omega_2} \langle \hat{U}_{i\mathbf{k}}^-(x_2) \hat{U}_{j\mathbf{k}}^{-*}(x'_2) \rangle \phi_{j\mathbf{k}}^-(x'_2) dx'_2 = \lambda_{\mathbf{k}}^- \phi_{i\mathbf{k}}^-(x_2), \quad (3.7)$$

in which the eigenfunctions are normalized by

$$\begin{aligned} (\phi_{i\mathbf{k}}^{+(n)}, \phi_{i\mathbf{k}}^{+(p)}) &= \delta_{np}, \\ (\phi_{i\mathbf{k}}^{-(n)}, \phi_{i\mathbf{k}}^{-(p)}) &= \delta_{np}. \end{aligned}$$

We redefine the inner product as

$$\begin{aligned} (\phi_{i_k}^{+(n)}, \phi_{i_k}^{+(n)})^+ &= \int_{\Omega_2} (\phi_{1_k}^{+(n)} \phi_{1_k}^{+(n)*} + \phi_{2_k}^{+(n)} \phi_{2_k}^{+(n)*}) dx_2, \\ (\phi_{i_k}^{-(n)}, \phi_{i_k}^{-(n)})^- &= \int_{\Omega_2} \phi_{3_k}^{-(n)} \phi_{3_k}^{-(n)*} dx_2. \end{aligned}$$

The Fourier-transformed velocity field of the plus- and minus-modes is now in the form

$$\mathbf{U}_k^+ = \begin{Bmatrix} \hat{u}_k^\parallel \\ \hat{v}_k \\ 0 \end{Bmatrix} = \sum_{n=1}^{\infty} a_k^{+(n)} \begin{Bmatrix} \phi_{1_k}^{+(n)} \\ \phi_{2_k}^{+(n)} \\ 0 \end{Bmatrix}, \quad (3.8)$$

$$\mathbf{U}_k^- = \begin{Bmatrix} 0 \\ 0 \\ \hat{u}_k^\perp \end{Bmatrix} = \sum_{n=1}^{\infty} a_k^{-(n)} \begin{Bmatrix} 0 \\ 0 \\ \phi_{3_k}^{-(n)} \end{Bmatrix}, \quad (3.9)$$

where the modal coefficients, $a_k^{+(n)}$ and $a_k^{-(n)}$, are

$$a_k^{+(n)} = (\mathbf{U}_k^+, \phi_{i_k}^{+(n)})^+, \quad (3.10)$$

$$a_k^{-(n)} = (\mathbf{U}_k^-, \phi_{i_k}^{-(n)})^-. \quad (3.11)$$

The incompressibility condition (3.5) and symmetries inherited in (3.1) and (3.2) imply that $\phi_{i_k}^{+(n)}$ needs to satisfy both the no-slip (or any linear) boundary condition and the divergence-free condition:

$$i|\mathbf{k}|\phi_{1_k}^{+(n)} + \frac{\partial \phi_{2_k}^{+(n)}}{\partial y} = 0, \quad (3.12)$$

whereas $\phi_{i_k}^{-(n)}$ needs to satisfy only the no-slip boundary condition.

Let us consider Waleffe's splitting (Waleffe 1995) again. It may be viewed as the projection of the plus- and minus-modes of the vector-valued POD modes (from the POD eigenvalue problem (2.1)) back onto the physical coordinate system:

$$\phi_{i_k,R} = \begin{bmatrix} k_x/|\mathbf{k}| & 0 & 0 \\ 0 & 1 & 0 \\ k_z/|\mathbf{k}| & 0 & 0 \end{bmatrix} \begin{Bmatrix} \phi_k^\parallel \\ \phi_{2_k} \\ 0 \end{Bmatrix}, \quad \phi_{i_k,S} = \begin{bmatrix} 0 & 0 & -k_z/|\mathbf{k}| \\ 0 & 0 & 0 \\ 0 & 0 & k_x/|\mathbf{k}| \end{bmatrix} \begin{Bmatrix} 0 \\ 0 \\ \phi_k^\perp \end{Bmatrix},$$

where ϕ_k^\parallel and ϕ_k^\perp are the horizontal components parallel and perpendicular to the wavenumber-vector of the POD eigenfunctions defined as in (3.1) and (3.2):

$$\phi_k^\parallel = \frac{k_x \phi_{1_k} + k_z \phi_{3_k}}{|\mathbf{k}|}, \quad \phi_k^\perp = \frac{-k_z \phi_{1_k} + k_x \phi_{3_k}}{|\mathbf{k}|}.$$

Inheriting the properties of the POD eigenfunctions, $\phi_{i_k,R}$ and $\phi_{i_k,S}$ are pairwise-orthogonal and divergence-free. However, unlike the PODS eigenfunction set, these basis functions are not optimal for plus- and minus-modes.

3.2. Statistical reconstruction of PODS

In order to probe the performance of the PODS eigenfunctions, we first consider the statistical reconstruction of the PODS eigenfunctions. Figure 3 shows the streamwise, wall-normal and spanwise components and twice the kinetic energy content in the first

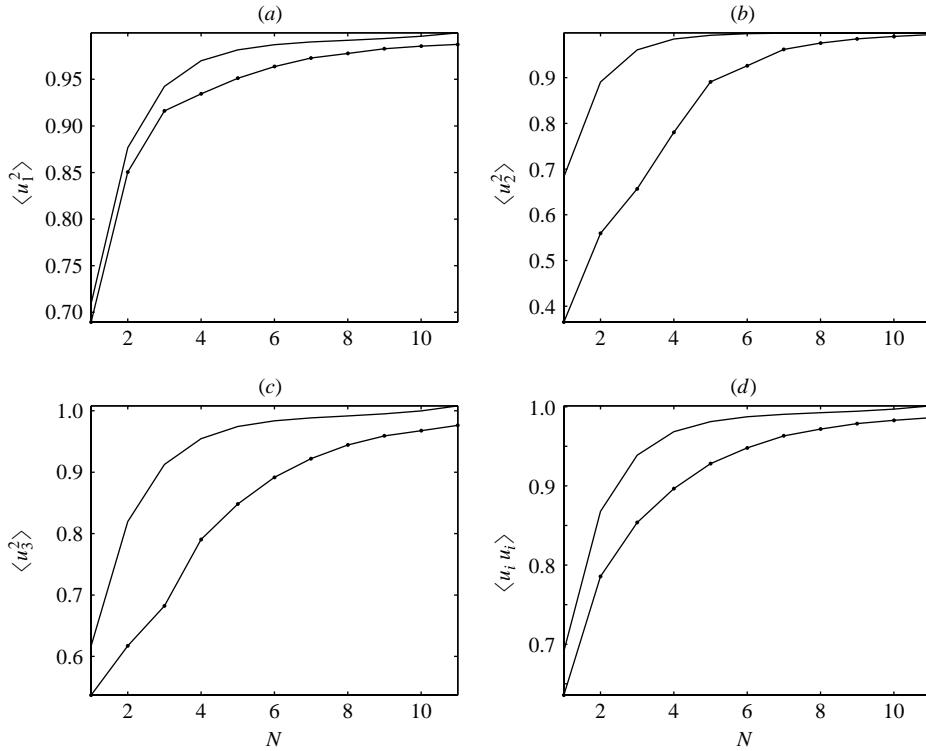


FIGURE 3. The streamwise, wall-normal and spanwise component energy and twice kinetic energy content across the localized domain ($x_2^+ \leq 84$) from localized POD and PODS reconstructions relative to the total energy content of the LES filtered field as a function of the number of eigenfunction families; solid, PODS; points, POD.

11 families of the *localized* POD and PODS across the localized ($x_2^+ \leq 84$) domain relative to the total component energy content in the LES filtered field. As figure 3(d) clearly reveals, PODS modes require approximately only two-thirds of the number of mode families to capture the same amount of energy content as do POD mode families. The drastic improvement of the PODS convergence rate in the component energy is, in fact, a consequence of the substantial improvement of the convergence rate in the lateral components as can be seen from figure 3(b) and 3(c). Because the POD itself is largely biased to the streamwise-component, the streamwise-component energy from the PODS expansion converges just slightly faster than that from the POD expansion.

To prevent any confusion we should emphasize at this point that this apparent faster convergence of PODS modes compared to standard POD modes with respect to the total energy has been bought at the expense of a doubling of the number of modes involved. In other words, in the case of the POD modes, a mode family includes the number of eigenfunctions that is equal to the number of Fourier modes present, but in the case of PODS modes, we have twice that number of eigenfunctions, because we have eigenfunctions describing both the plus- and the minus-modes. Thus, the ‘net-convergence’, taking into account the total number of eigenfunctions needed to represent the velocity field to a given accuracy in the energy, is indeed slower for the PODS modes than for the standard POD modes. This is as it should be, since

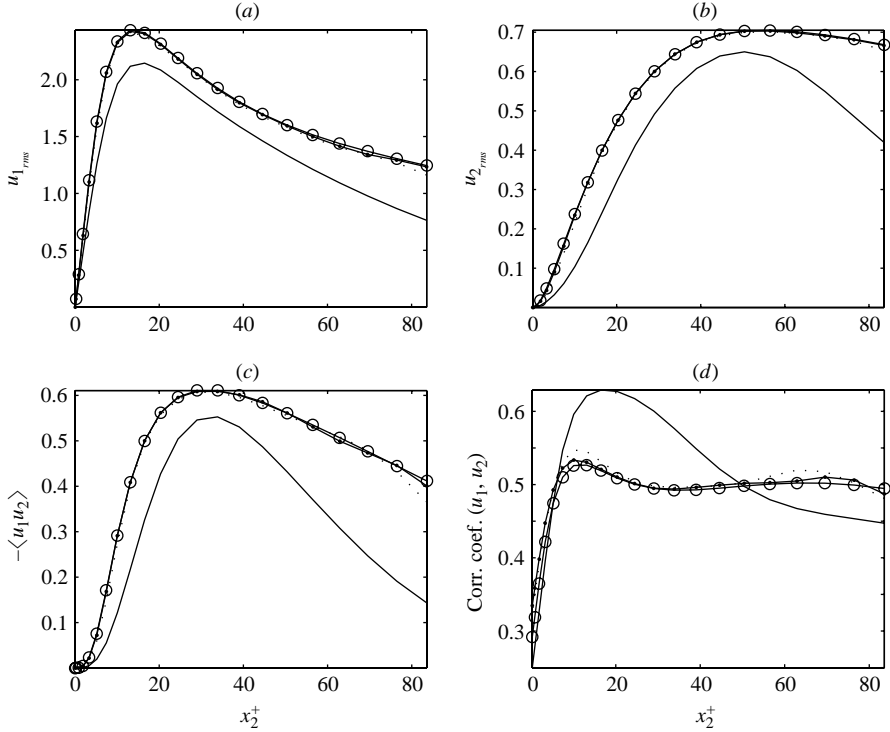


FIGURE 4. Statistical reconstruction from the localized ($0 \leq x_2^+ \leq 84$) PODS eigenfunctions: (a) streamwise turbulent intensity, (b) wall-normal turbulent intensity, (c) Reynolds shear stress and (d) correlation coefficient of streamwise and wall-normal velocity; solid, $N=1$; dotted, $N=4$; points, $N=6$; circles, LES.

we can prove that no other set of eigenmodes can show faster convergence, in the energy norm, than the standard POD modes. Nevertheless, as we will show below, PODS modes have favourable properties over standard POD modes with regard to modelling the dynamics of the turbulent flow.

Figures 4(a), 4(b), 4(c) and 4(d) show the statistical reconstruction of the streamwise and wall-normal turbulent intensity, Reynolds shear stress and the correlation coefficient of streamwise and wall-normal velocity from the localized PODS eigenfunctions in the region $0 \leq x_2^+ \leq 84$ against the statistics from the LES *filtered* velocity field. As expected, the streamwise turbulent intensity reconstruction from the PODS expansion is only slightly better than that from the POD expansion, as shown in figure 4(a). The structures of the wall-normal (and spanwise, see Juttijudata (2003)) turbulent intensity from the PODS eigenfunctions, on the other hand, improve significantly compared to figure 2(b). Only 4 families of PODS modes are needed to almost fully reproduce the LES wall-normal turbulent intensity except for a small under-reproduction in the regions $x_2^+ \leq 20$ and $x_2^+ \geq 75$. The Reynolds shear stress reconstruction from the PODS eigenfunctions also converges (more or less) monotonically to the resolved LES Reynolds shear stress, unlike that from the POD eigenfunctions as shown in figure 4(c). The first 4 PODS families are sufficient to almost fully reproduce the stress. The correlation coefficient of streamwise and wall-normal velocity shown in figure 4(d) again emphasizes the superiority of the PODS eigenfunctions over the POD eigenfunctions. Again, the first 4 families of PODS are enough to capture all of the

N	1	4	6	8	11
POD	29.17	69.55	77.62	82.67	87.94
PODS	32.16	77.54	87.17	92.57	96.58

TABLE 1. Percentage of energy content across the channel in the first N families of POD and PODS modes in the full channel domain. For each POD and PODS family, the energies are summed over all Fourier modes. The table shows the order, and energy percentage across the channel in POD and PODS modes.

Order	(l, m, n)	λ	λ^+	λ^-	Degeneracy	% Energy
1	$(\pm 1, \pm 2, 1)$	9.8184	1.0687	8.7497	4	3.9694
2	$(\pm 1, \pm 1, 1)$	7.4348	1.0443	6.3905	4	3.0058
3	$(0, \pm 1, 1)$	14.8535	0.7953	14.0581	2	3.0025
4	$(\pm 1, \pm 3, 1)$	7.2845	0.6741	6.6103	4	2.9450
5	$(\pm 1, \pm 3, 2)$	6.4577	0.5956	5.8621	4	2.6107
6	$(\pm 1, \pm 2, 2)$	6.3714	0.5994	5.7720	4	2.5758
7	$(\pm 1, \pm 1, 2)$	6.3323	1.0263	5.3060	4	2.5600
8	$(\pm 1, \pm 4, 1)$	6.2872	0.5852	5.7021	4	2.5418
9	$(\pm 1, \pm 4, 2)$	5.2958	0.4984	4.7974	4	2.1410
10	$(\pm 2, \pm 2, 1)$	4.7291	0.7670	3.9621	4	1.9119

TABLE 2. The empirical eigenvalues of the first 10 dominant PODS modes in the full channel domain. The table shows the order (integer harmonic) Fourier-PODS mode, its total, + mode, - mode eigenvalues, its degeneracy, and its percentage of total average energy across the channel.

key structures of the correlation coefficient. The over-reproduction of correlation coefficient in the $x_2^+ \leq 20$ and $x_2^+ \approx 50-80$ regions is the consequence of the directional preference of the plus-mode eigenfunctions to the lateral motion at the maximum lateral component energy location, $x_2^+ \approx 30$, and that of the minus-mode eigenfunctions to the streamwise motion at the maximum streamwise component energy location, $x_2^+ = 13$.

3.3. Empirical eigenvalues and eigenfunctions

Let us now consider the eigenvalues and eigenfunctions of the PODS. In contrast to §3.2, we will consider the eigenvalues and eigenfunctions in the full channel domain, i.e. we set $\Omega_2 \in [-1, 1]$ in (3.6), (3.7) and the inner products. These eigenfunctions will be used later as a basis for our full channel dynamical models.

Table 1 shows the percentage of energy content across the channel from different numbers of POD and PODS families. The energies are summed over all Fourier modes for each POD and PODS family. The first families of POD and PODS modes capture about the same energy content (30 % and 32 %, respectively). For the higher-order families, the PODS modes require approximately two-third of the number of POD eigenfunction families to capture the same amount of energy content.

Table 2 shows the eigenvalues of the first 10 dominant PODS modes in the full channel domain (recalling that the symmetries in §2.1 force certain degeneracies on the eigenfunctions). The most energetic mode residing in $(l, m, n) = (\pm 1, \pm 2, 1)$, where l and m denote harmonics of the fundamental wavenumber, carries only 4 %, and the first 10 modes contain only 28 %, of the total energy content across the channel, in contrast to the localized PODS modes (see Juttijudata 2003) that carry up to 8 % of the energy content across the localized domain ($x_2^+ \leq 84$) in the first eigenmode,

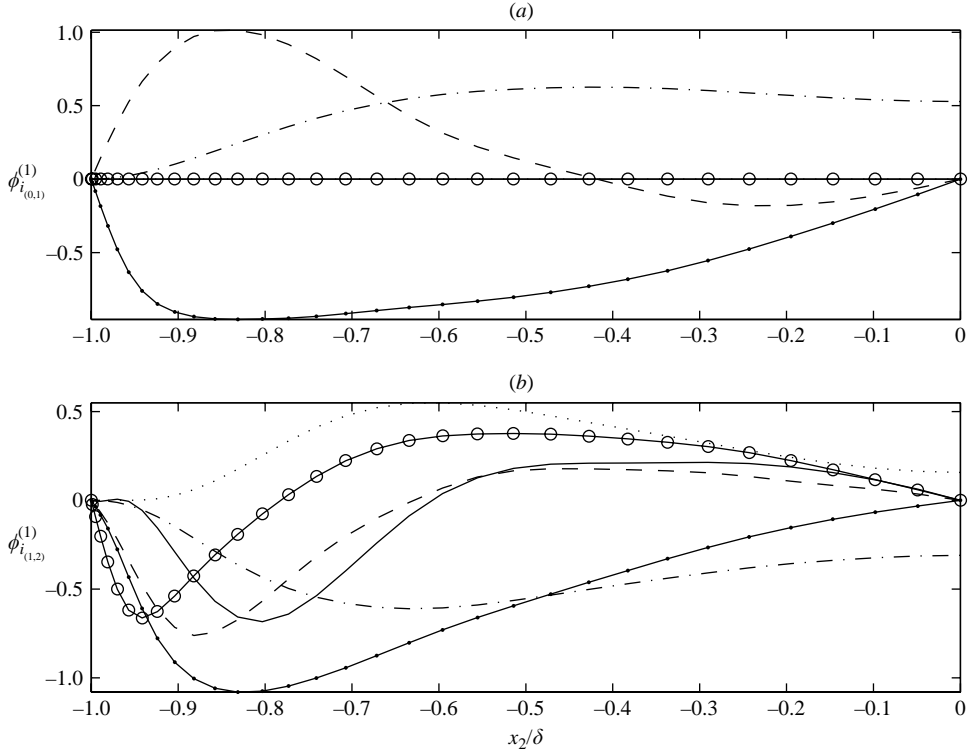


FIGURE 5. Empirical eigenfunctions in the wall-to-wall domain. (a) (1,2,1), (b) (0,1,1) (integer harmonic) Fourier–PODS modes: solid, $\text{Re}(\phi_1^+)$; dashed, $\text{Im}(\phi_1^+)$; dash-dot, $\text{Re}(\phi_2^+)$; dotted, $\text{Im}(\phi_2^+)$; points, $\text{Re}(\phi_3^-)$; circles, $\text{Im}(\phi_3^-)$.

and carry up to 50% of the energy content in the first 10 eigenmodes. The PODS eigenfunctions of the full channel domain clearly converge more slowly than those of the localized domain. We may estimate the length scale of the coherent structures from the eigenvalues. The most energetic mode (including its degeneracies) resides in $(\pm 1, \pm 2, 1)$. This suggests that the coherent structures reconstructed from the PODS expansion are approximately $1650 \nu/u_\tau$ long in the streamwise direction and $275 \nu/u_\tau$ wide in the spanwise direction. This is comparable to the length scales found in physical structures of turbulent boundary layers.

Figure 5 shows the profile of the PODS eigenfunctions in the full channel domain of (1,2,1) and (0,1,1) (integer harmonic) Fourier–PODS modes as a function of the wall distance (from the lower wall to the centreline of the channel). Notice that the eigenfunctions satisfy the no-slip condition at the wall, $\phi_i^\pm(x_2/\delta = -1) = 0$, and the slope of ϕ_2^+ at the wall satisfies both the no-slip and the incompressibility condition, $d\phi_2^+/dx_2(x_2/\delta = -1) = 0$. The reconstruction of eigenfunctions in physical space (see Juttijudata 2003) also exhibits the structures of streaks and streamwise vortices.

4. Derivation of dynamical model

4.1. Equations for coherent structures

We only outline the derivation of the equations for coherent structures. The detailed derivation can be found in Holmes *et al.* (1996). We use the conventional tensor

notation, with summation implied on repeated indices (Einstein notation). The dynamical equations of the mean and fluctuating velocity (including the contribution from both coherent and incoherent motions at this point) may be derived by introducing the Reynolds decomposition, $v_i = \langle v_i \rangle + u_i$, $\pi = \langle \pi \rangle + p$, into the Navier–Stokes equations. We further substitute the decomposition $u_i = u_{i<} + u_{i>}$, where $u_{i<}$ and $u_{i>}$ denote resolved and unresolved velocity (representing the coherent and incoherent motions), into the fluctuating velocity equations and project them onto the subspace of the resolved modes. By assuming that the operations of the projection and differentiation commute, we obtain the dynamical equations of coherent structures:

$$\frac{\partial u_{i<}}{\partial t} = N_{i<} + \nu u_{i,jj<} - p_{,i<}, \quad (4.1)$$

where

$$N_{i<} = -\frac{1}{2}\{u_{2<}U_{1,2} + (u_{j<}U_{1,j})_{<}\delta_{i1} - \frac{1}{2}\{u_{i,1<}U_1 + (u_{i<}U_{1,1})_{<}\} \\ - \frac{1}{2}\{(u_{i,j<}u_{j<} + (u_{i<}u_{j<})_{,j}) - (\langle u_{1,j<}u_{j<} \rangle + \langle u_{1<}u_{2<},2 \rangle)\delta_{i1}\}_{<} - (\tau_{ij,j>})_{<},$$

and

$$\tau_{ij,j>} = \frac{1}{2}\{u_{2>}U_{1,2} + (u_{j>}U_{1,j})_{,j}\delta_{i1} + \frac{1}{2}\{u_{i,1>}U_1 + (u_{i>}U_{1,1})_{,1}\} \\ + \frac{1}{2}\{(u_{i,j<}u_{j>} + u_{i,j>}u_{j<} + u_{i,j>}u_{j>} + (u_{i<}u_{j>} + u_{i>}u_{j<} + u_{i>}u_{j>})_{,j}) \\ - (\langle u_{1,j<}u_{j>} + u_{1,j>}u_{j<} + u_{1,j>}u_{j>} \rangle + \langle u_{1<}u_{2>} + u_{1>}u_{2<} + u_{1>}u_{2>},2 \rangle)\delta_{i1}\}. \quad (4.2)$$

Substituting the decomposition into the mean velocity equations we obtain

$$\frac{\partial U_1}{\partial t} = -\frac{1}{2}(\langle u_{1,j<}u_{j<} \rangle + \langle u_{1<}u_{2<},2 \rangle) - \langle \tau_{12>},2 \rangle + \nu U_{1,22} - P_{,1}. \quad (4.3)$$

In order to close the dynamical equations, we need to specify $\tau_{ij>}$ as a function of the resolved motion, which will be discussed in §4.3.

Note that the nonlinear terms in (4.1) and (4.3) are in *skew-symmetric* form. The angle bracket denotes the spatial average defined by

$$\langle f \rangle = \frac{1}{L_1 L_3} \int_0^{L_1} \int_0^{L_3} f(\mathbf{x}, t) dx_3 dx_1.$$

We denote $\langle v_i \rangle = U_i$, and $\langle \pi \rangle = P$. By definition, $\langle f \rangle$ is a function of x_2 alone.

The continuity equation of the fluctuating velocity is given by

$$u_{i<,i} = 0. \quad (4.4)$$

The periodic and no-slip boundary condition of (4.1) are

$$u_{i<}(x_1, x_2, x_3 + L_3, t) = u_{i<}(x_1 + L_1, x_2, x_3, t) = u_{i<}(x_1, x_2, x_3, t), \\ u_{i<}(x_1, \pm 1, x_3, t) = 0,$$

respectively, and the no-slip boundary condition of (4.3) is

$$U_i(\pm 1, t) = 0.$$

We impose a periodic boundary condition on the fluctuating velocity field by expanding the fluctuating velocity field in the Fourier modes (the empirical eigenfunctions in homogeneous directions). The no-slip conditions at both walls are automatically satisfied by the eigenfunctions. For the mean velocity equations, the no-slip conditions must be imposed explicitly.

The Fourier-transformed equations of coherent structures (4.1) and divergence-free conditions (4.4), respectively, are

$$\frac{\partial \hat{u}_{i_{k<}}}{\partial t} = \hat{N}_{i_{k<}} + v \left(-|\mathbf{k}|^2 + \frac{\partial^2}{\partial x_2^2} \right) \hat{u}_{i_{k<}} - \Omega_i \hat{p}_{k<}, \quad (4.5)$$

$$ik_1 \hat{u}_{1_{k<}} + \frac{\partial}{\partial x_2} \hat{u}_{2_{k<}} + ik_3 \hat{u}_{3_{k<}} = 0, \quad (4.6)$$

where $\hat{N}_{i_{k<}}$ is the Fourier transform of the nonlinear terms. The spatial derivative operator Ω_i is defined as

$$\Omega_i \hat{p}_{k<} = \begin{cases} ik_1 \hat{p}_{k<} & \text{if } i = 1, \\ \frac{\partial}{\partial x_2} \hat{p}_{k<} & \text{if } i = 2, \\ ik_3 \hat{p}_{k<} & \text{if } i = 3. \end{cases} \quad (4.7)$$

Let us apply Squire's transformation to the dynamical equations. Recalling that u^{\parallel} and u^{\perp} are the horizontal Fourier-transformed velocity components parallel and perpendicular to the wavenumber-vector, and v is that normal to the wall, the equations in Squire's coordinate system are

$$\left. \begin{aligned} \frac{\partial u^{\parallel}_{<}}{\partial t} &= N^{\parallel}_{<} + v \left(-|\mathbf{k}|^2 + \frac{\partial^2}{\partial x_2^2} \right) u^{\parallel}_{<} - i|\mathbf{k}|p_{<}, \\ \frac{\partial v_{<}}{\partial t} &= N^v_{<} + v \left(-|\mathbf{k}|^2 + \frac{\partial^2}{\partial x_2^2} \right) v_{<} - \frac{\partial}{\partial x_2} p_{<}, \\ \frac{\partial u^{\perp}_{<}}{\partial t} &= N^{\perp}_{<} + v \left(-|\mathbf{k}|^2 + \frac{\partial^2}{\partial x_2^2} \right) u^{\perp}_{<}, \end{aligned} \right\} \quad (4.8)$$

and

$$i|\mathbf{k}|u^{\parallel}_{<} + \frac{\partial}{\partial x_2} v_{<} = 0, \quad (4.9)$$

where $N^{\parallel}_{<}$ and $N^{\perp}_{<}$ are the Fourier transforms of the components of the nonlinear terms in (4.5) that are parallel and perpendicular to the wavenumber vector, and $N^v_{<}$ is that which is normal to the wall. For the sake of brevity, we have dropped the hats and the subscript \mathbf{k} from (4.8) and (4.9). Notice that Squire's transformation removes the pressure term from u^{\perp} .

4.2. Galerkin projection

The procedure of Galerkin projection of (4.8) onto the PODS basis functions is similar to that of (4.5) onto the POD basis functions except this time the projection has to be performed twice:

$$\left(\left(\begin{array}{c} \frac{\partial u^{\parallel}_{<}}{\partial t} \\ \frac{\partial v_{<}}{\partial t} \\ 0 \end{array} \right), \left(\begin{array}{c} \phi_1^{(n)+} \\ \phi_2^{(n)+} \\ 0 \end{array} \right) \right)^+ = \left(\left(\begin{array}{c} N^{\parallel}_{<} + \dots \\ N^v_{<} + \dots \\ 0 \end{array} \right), \left(\begin{array}{c} \phi_1^{(n)+} \\ \phi_2^{(n)+} \\ 0 \end{array} \right) \right)^+,$$

for plus-modes, and

$$\left(\left\{ \begin{array}{c} 0 \\ 0 \\ \frac{\partial u_{\leq}^{\perp}}{\partial t} \end{array} \right\}, \left\{ \begin{array}{c} 0 \\ 0 \\ \phi_3^{(n)-} \end{array} \right\} \right)^{-} = \left(\left\{ \begin{array}{c} 0 \\ 0 \\ N_{<}^{\perp} + \dots \end{array} \right\}, \left\{ \begin{array}{c} 0 \\ 0 \\ \phi_3^{(n)-} \end{array} \right\} \right)^{-},$$

for minus-modes. The final dynamical model in the PODS subspace is

$$\frac{da^{+(n)}}{dt} = \mathcal{N}^{+(n)} + \nu L_{np}^{+} a^{+(n)} + d^{+(n)}, \quad (4.10)$$

$$\frac{da^{-(n)}}{dt} = \mathcal{N}^{-(n)} + \nu L_{np}^{-} a^{-(n)}. \quad (4.11)$$

The nonlinear terms are given by

$$\begin{aligned} \mathcal{N}^{+(n)} &= \int_{-1}^{X_2} (N_{<}^{\parallel} \phi_1^{+(n)*} + N_{<}^{\nu} \phi_2^{+(n)*}) dx_2, \\ \mathcal{N}^{-(n)} &= \int_{-1}^{X_2} N_{<}^{\perp} \phi_1^{-(n)*} dx_2, \end{aligned}$$

and the linear model coefficients are given by

$$\begin{aligned} L_{np}^{+} &= -|\mathbf{k}|^2 \delta_{np} - \int_{-1}^{X_2} \left(\frac{d\phi_1^{+(p)}}{dx_2} \frac{d\phi_1^{+(n)*}}{dx_2} + \frac{d\phi_2^{+(p)}}{dx_2} \frac{d\phi_2^{+(n)*}}{dx_2} \right) dx_2 \\ &\quad + \left[\frac{d\phi_1^{+(p)}}{dx_2}(X_2) \phi_1^{+(n)*}(X_2) + \frac{d\phi_2^{+(p)}}{dx_2}(X_2) \phi_2^{+(n)*}(X_2) \right], \\ L_{np}^{-} &= -|\mathbf{k}|^2 \delta_{np} - \int_{-1}^{X_2} \frac{d\phi_3^{-(p)}}{dx_2} \frac{d\phi_3^{-(n)*}}{dx_2} dx_2 + \left[\frac{d\phi_3^{-(p)}}{dx_2}(X_2) \phi_3^{-(n)*}(X_2) \right]. \end{aligned}$$

Note that instead of substituting the velocity expansion in the nonlinear terms and computing the nonlinear coefficients like Aubry *et al.* (1988), we compute the product of the nonlinear terms in the physical space, transform the nonlinear terms to the Fourier space and project each Fourier coefficient of nonlinear terms onto the PODS subspace. The main advantage of this approach is that we do not have to derive the nonlinear model coefficients again when we change the form of the nonlinear terms or the closure model of the unresolved stresses.

The pressure source terms are defined as

$$d^{+(n)} = \int_{-1}^{X_2} \left(i\mathbf{k} p_{<} \phi_1^{+(n)} + \frac{dp_{<}}{dx_2} \phi_2^{+(n)} \right) dx_2.$$

We may apply the divergence theorem and use the incompressibility condition to rearrange the pressure source terms as

$$d^{(n)+} = -p_{<}(X_2) \phi_2^{+(n)*}(X_2).$$

In the full channel, $X_2 = 1$, the eigenfunctions satisfy the no-slip conditions; therefore the contributions from the boundary terms in the square brackets $[\cdot]$ of the linear model coefficients and from the pressure source terms are exactly zero. Furthermore, the well-posedness of the model is ensured. In contrast, in the localized domain model of Aubry *et al.* (1988), neither of these terms is zero, nor is the well-posedness

of the model ensured as pointed out in Zhou & Sirovich (1992). The issue of the well-posedness of the localized model results from replacing three velocity boundary condition in the Navier–Stokes equations with a single pressure term in the model. As an alternative, Zhou & Sirovich (1992) propose constructing the localized low-dimensional model by using artificially localized POD eigenfunctions obtained from a linear combination of the full channel POD eigenfunctions. Alternatively, Gibson (2002) imposes the velocity boundary condition onto the localized domain model via the tau-method projection (see Canuto *et al.* 1988). Unfortunately, his model suffers from instability. The reader is directed to Zhou & Sirovich (1992), Berkooz *et al.* (1994), Sirovich & Zhou (1994), Holmes *et al.* (1996) and Gibson (2002) for further discussion on the well-posedness and the boundary condition of localized models. In order to avoid an unreliable ad hoc model of the pressure source term and the issue of the well-posedness of the model, we will consider the full channel domain in this study. We now set $\Omega_2 \in [-1, 1]$ in (3.6), (3.7), and the inner products and $X_2 = 1$ in the model coefficients in (4.10) and (4.11), in order to obtain full channel PODS eigenfunctions and dynamical models.

4.3. Interaction with unresolved modes

In the classical view of turbulence, turbulence energy is primarily produced and transported by large-scale motions. Energy cascades from large-scales to smaller scales by vortex stretching in the nonlinear terms, and eventually dissipates in the smallest (Kolmogorov) scales through a viscous mechanism (see Tennekes & Lumley 1972). Turbulence is an inviscid, inertial phenomenon that is controlled by the large-scale motions (represented by the low-order eigenfunctions), and is uninfluenced by the exact nature of the viscous mechanism (represented by high-order eigenfunctions which are usually truncated in low-dimensional models). Clearly the exact nature of the unresolved stress model is not important as long as it prevents an artificial energy accumulation in the unresolved-scale motions resulting from the interruption of the natural energy cascade process. Aubry *et al.* (1988) model the unresolved motion with a Heisenberg spectral transfer model (Heisenberg 1948) or equivalently an eddy-viscosity model or Smagorinsky SGS model in LES (Smagorinsky 1963). Rempfer (1993) and Ma & Kardianakis (2002) model the unresolved stress by more complex, independent eddy-viscosity models for each POD mode. Both models successfully reproduce the qualitative pictures of turbulence events. The constant eddy-viscosity model is also used in the quantitative simulation of Omurtag & Sirovich (1999) and Gibson (2002). Gibson (2002) also studies the performance of eddy-viscosity models in the quantitative model and suggests a deficiency of the constant eddy-viscosity models. From our point of view, in order to obtain good quantitative models, the unresolved stress model should account for the effect of the unresolved motion in turbulence production, transport and pressure redistribution in the coherent motion equations, as well as in the Reynolds shear stress in the mean motion equation. In our study, we adopt the dynamic Smagorinsky and one-coefficient mixed model from LES (e.g. Sarghini *et al.* 1999) for the unresolved stress model. Note that the filtering operator in the dynamic procedure is used in the horizontal directions only.

The plane-averaged formulation of the dynamic Smagorinsky model is

$$\tau_{ij>} - \frac{\tau_{kk>}}{3}\delta_{ij} = -2C_{ev}|S_{<}|\Delta^2 S_{ij<}, \quad C_{ev}(x_2, t) = -\frac{1}{2} \frac{\langle \mathcal{L}_{ij} M_{ij} \rangle}{\langle M_{ij} M_{ij} \rangle}, \quad (4.12)$$

and the plane-averaged formulation of the dynamic one-coefficient mixed model is

$$\tau_{ij>} = A_{ij} - 2C_{ev}|S_{<}|\Delta^2 S_{ij<}, \quad C_{ev}(x_2, t) = -\frac{1}{2} \frac{\langle \mathcal{L}_{ij} M_{ij} \rangle - \langle N_{ij} M_{ij} \rangle}{\langle M_{ij} M_{ij} \rangle}, \quad (4.13)$$

where

$$\begin{aligned} A_{ij} &= \overline{\overline{u_i u_j}} - \overline{u_i} \overline{u_j}, \\ \mathcal{L}_{ij} &= \widetilde{\widetilde{u_i u_j}} - \widetilde{u_i} \widetilde{u_j}, \\ M_{ij} &= \overline{\Delta}^2 [(\widetilde{\Delta}/\overline{\Delta})^2 |\widetilde{S}| \widetilde{S}_{ij} - |\overline{S}| \overline{S}_{ij}], \\ N_{ij} &= B_{ij} - \widetilde{A}_{ij}, \end{aligned}$$

and

$$B_{ij} = \widetilde{\widetilde{u_i u_j}} - \widetilde{u_i} \widetilde{u_j}.$$

The top-hat filter is used for all explicit filtering operations required for the evaluation of the scale-similar model and as a test filter. The overbar and tilde denote the filtering operation with filter widths in the streamwise and spanwise directions of $\overline{\Delta}$ and $\widetilde{\Delta}$, respectively, where $\widetilde{\Delta}/\overline{\Delta} = \sqrt{6}$ as suggested by Lund (1998).

We may expect that the unresolved stresses from the Smagorinsky (or the eddy-viscosity type) model provides enough additional energy dissipation to the truncated systems but are poorly correlated to the exact unresolved stresses from the full system, if we assume the behaviour of the unresolved stresses in the dynamical system is similar to that of the SGS in LES. The introduction of a scale-similar part in the mixed model should improve the correlation of the unresolved stresses from the model and that from the full system (see Bardina, Ferziger & Reynolds 1983). Note that because we assume the scale-similarity and perform a double filtering operation in the dynamic procedure only in the horizontal directions, we expect the unresolved stress models may fail to accurately account for the interaction with unresolved motion in the wall-normal direction.

5. Numerical simulations

The dynamical model is integrated in time using a Fourier–PODS pseudo-spectral method. The nonlinear term is cast in skew-symmetric form and computed without de-aliasing. The empirical eigenfunctions are projected on the Chebyshev collocation points, $x_2^j/\delta = \cos(\pi/(N_2 - 1) \times (j - 1))$, where $j = 1, \dots, N_2$, and represented using cubic spline interpolation. The second-order derivatives of the function are prescribed at both boundary points, $x_2/\delta = \pm 1$, in order to calculate the spline coefficients. The derivatives are estimated using second-order one-sided finite differences. The differentiation and integration in the wall-normal direction are therefore based on cubic spline interpolation. Here we choose to represent the basis functions using cubic spline interpolation instead of Chebyshev polynomials, which are more accurate, because the cubic spline interpolation offers a great flexibility to represent the basis functions in different domain sizes (e.g. the full channel domain ($-1 \leq x_2 \leq 1$) and localized domain considered earlier ($0 \leq x_2^+ \leq 84$)). At this point we are more interested in the convergence rate of the basis functions and their dynamical models than in the numerical methods and efficiency. In our simulations, we choose $N_2 = 65$. This number equals the resolution of a well-resolved LES and ensures that all the eigenfunctions

	Basis function	Truncation	$\tau_{>ij}$	Re_τ
P6	POD	($\pm 16, \pm 24, 4$)	$e = 0.0$	212
P8	POD	($\pm 16, \pm 24, 6$)	$e = 0.0$	214
S4	PODS	($\pm 16, \pm 24, 4$)	$e = 0.0$	179
SC	PODS	($\pm 16, \pm 24, 4$)	$e = 0.8$	147
DS	PODS	($\pm 16, \pm 24, 4$)	Smagorinsky	174
DM	PODS	($\pm 16, \pm 24, 4$)	mixed model	172
LES	–	(32, 65, 48)	mixed model	172
CDNS	–	(32, 65, 48)	–	180

TABLE 3. Simulation parameters and frictional Reynolds number: the basis function (integer harmonic) Fourier–PODS truncation ((N_1, N_2, N_3) in LES and CDNS), unresolved stress model and friction Reynolds number.

in our simulations are well-resolved on the grids as seen in figure 5. The time-advancement is performed by a semi-implicit low-storage third-order Runge–Kutta time-stepping scheme (Spalart *et al.* 1991). We constantly change the size of the time step in order to achieve the maximum allowable CFL, $0.8 \times CFL_{max} = 0.8 \times \sqrt{2.8}$. Eventually the system of linear equations in each Fourier mode is solved by Gauss elimination with scaling and partial pivoting. A fixed volume flow rate is maintained throughout the simulation. Because the mean mode representation is excluded from the PODS basis functions, the mean velocity equation is discretized by a second-order central finite difference scheme in the wall-normal direction and advanced in time using the same Runge–Kutta time-stepping scheme. The computational parameters in the dynamical model are the same as in the LES database: the Reynolds number based on laminar centreline velocity, U_c , and half-channel width, δ , of 4000, equivalent to 172 based on *computed* friction velocity, u_τ ; the computational domain size normalized by the half-channel width of $(L_1, L_2, L_3) = (3\pi, 2, \pi)$, equivalent to $(L_1^+, L_2^+, L_3^+) = (1640, 348, 547)$; $(N_1, N_2, N_3) = (32, 65, 48)$, equivalent to $(\Delta x_1^+, \Delta x_2^+, \Delta x_3^+) \approx (50, 0.2, 11)$ based on the LES friction velocity.

A set of eight simulations will be compared in §6. Three of the simulations are dynamical models based on 6 and 8 POD families (P6 and P8) and 4 PODS families (S4) with no unresolved stress model. We choose to compare S4 to P6 and P8. According to table 1, S4 and P6 contain approximately the same amount of energy, 78 % of total energy content, which suggests the convergence rate of S4 and P6, in an energy sense, are comparable. The comparison of S4 and P6 should therefore be a good indication of the relative performance of PODS and POD models for a given energy content. In terms of computational resource, the number of unknowns in the PODS expansion, $a^{(n)+}$ and $a^{(n)-}$, is twice of that in the POD expansion, $a^{(n)}$. Therefore the comparison between S4 and P8 containing 83 % of total energy content is quite reasonable in terms of computational resource. An additional three computations we present were done as dynamical simulations based on 4 PODS families using a constant eddy-viscosity (SC), dynamic Smagorinsky (DS) and one-coefficient mixed model (DM). The last two simulations are LES with a dynamic one-coefficient mixed SGS model (LES) and a coarse-grid direct numerical simulation (CDNS). The main parameters for all the simulations are shown in table 3: the truncation of PODS (and POD) modes, the unresolved stress model, and the friction Reynolds number.

The statistically stationary velocity field from the one-coefficient mixed SGS model LES is projected onto PODS (or POD) subspace and integrated in time until the

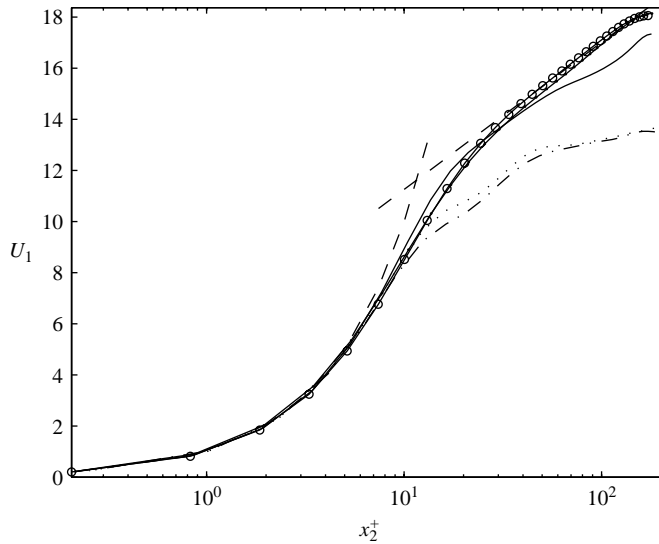


FIGURE 6. Mean velocity profiles from simulations: solid, S4 (4-family PODS); dotted, P6 (6-family POD); dash-dot, P8 (8-family POD); points, CDNS (coarse-grid DNS); circles, LES; dashed, law of wall.

flow reaches the statistically stationary state defined by a linear profile of total shear stress. The flow is further integrated in time to obtain a running time average of the statistics. The statistical calculations are based on 500 independent samples for P6, P8, S4, SC and CDNS, and 1500 independent samples for DS, DM and LES. The number of samples is increased by averaging over horizontal (homogeneous) planes.

6. Results

6.1. Comparison to POD basis functions

In order to obtain reasonably accurate statistics, we retain up to 4 PODS families (S4). We also integrated the 6- and 8-family PODS models (not included here) and found no qualitative difference in statistics and velocity structures between these models and the 4-family PODS model. The difference between model statistics and LES statistics (with SGS contribution) reduces monotonically as the number of families increases. In order to make a fair comparison to POD models, we will consider 6 and 8 POD family models (P6 and P8). For the sake of comparison, we also plot the statistics of the coarse-grid DNS (CDNS).

Figure 6 shows the mean velocity profiles from different models as a function of the wall distance. Dashed lines in the figure represent the mean velocity profile from the linear law of the wall and the log law. The most accurate prediction of the mean velocity profile among S4, P6 and P8 is obtained with S4. The intercept of the log layer from S4 is very close to that from LES and the law-of-the-wall prediction, whereas that from P6 and P8 are too low, consistent with the higher friction Reynolds numbers as shown in table 3. The accurate prediction of mean velocity from S4 is a consequence of an accurate prediction of Reynolds shear stress as can be seen in figure 7(c).

Figure 7(a) shows the streamwise turbulent intensity reproduced from different models as a function of the wall distance. Note that the intensity from LES includes both the resolved stresses and SGS. P6, P8 and S4 produce a qualitatively close

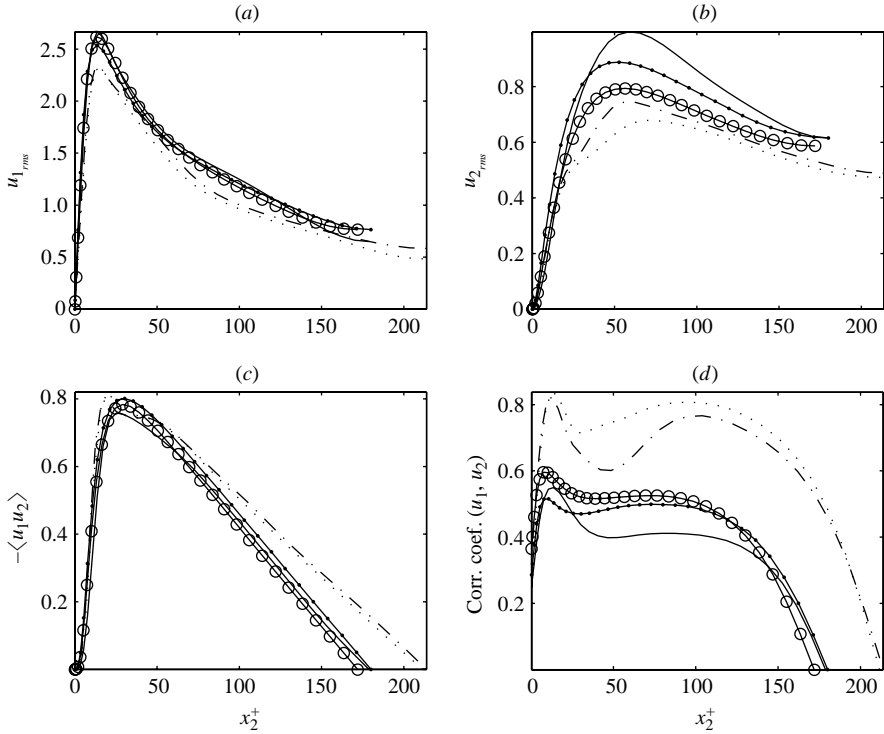


FIGURE 7. Statistics from simulations: (a) streamwise turbulent intensity, (b) wall-normal turbulent intensity, (c) Reynolds shear stress and (d) correlation coefficient of streamwise and wall-normal velocity: solid, S4 (4-family PODS); dotted, P6 (6-family POD); dash-dot, P8 (8-family POD); points, CDNS (coarse-grid DNS); circles, LES.

prediction of the distribution of the intensity, especially below $x_2^+ \leq 100$, and capture the location of maximum intensity fairly well. Nevertheless, only S4 could accurately reproduce the maximum intensity. We may obtain an accurate maximum intensity from P6 and P8, if we renormalize their intensities and wall distances by the LES friction velocity. This suggests that the shape of streamwise turbulent intensity from POD and PODS models is predominantly controlled by the characteristics of the empirical data used to generate POD and PODS eigenfunctions whereas the level of maximum intensity is controlled by the turbulence production mechanism (depending on the accuracy of the mean velocity profile and Reynolds shear stress prediction). The bias of streamwise turbulent intensity prediction toward the characteristics of the empirical data is again evident in a better prediction from S4 than that from CDNS in the wall region, $x_2^+ \leq 40$, where both models produce relatively accurate production levels.

Figure 7(b) shows the prediction of the wall-normal turbulent intensity from different models. It is inconclusive whether the intensity profile from S4 is better than that from P6 and P8. S4 over-predicts the maximum intensity and pushes the location of maximum intensity further away from the wall by approximately 10 wall units. Since the actual peak and its location of wall-normal intensity is controlled by the low-order resolved eigenmodes, the shifting of the peak and its location in S4 suggest an anomalous activity of higher-order resolved eigenmodes that probably results from energy accumulation in the higher-order resolved modes. Nevertheless, the intensity profile from S4 is much smoother than that from P6 and P8 which, in

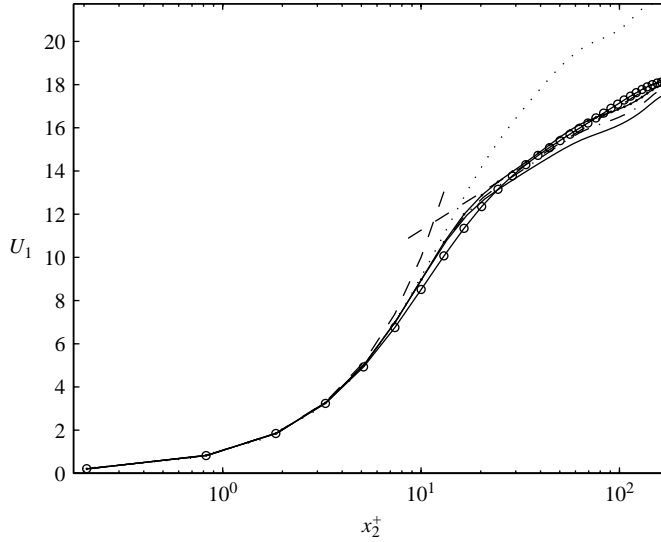


FIGURE 8. Mean velocity profiles from simulations: solid, S4 (no unresolved stress model); dotted, SC (constant eddy-viscosity); dash-dot, DS (dynamic Smagorinsky model); points, DM (dynamic mixed model); circles, LES; dashed, law of wall.

turn, improves the Reynolds shear stress profile in figure 7(c). We may draw the same conclusion from the spanwise turbulent intensity reconstruction (see Juttijudata 2003).

Figure 7(c) shows the reproduction of the Reynolds shear stress from different models as a function of the wall distance. Evidently, S4 can reproduce the smooth profile of the Reynolds shear stress more accurately than either P6 or P8. The correlation coefficients of the streamwise and wall-normal velocity of different models are shown in figure 7(d). Overall, the prediction from S4 is much better than that from P6 and P8. However, S4 considerably under-predicts the correlation coefficient by 25 % in the region $30 \leq x_2^+ \leq 100$.

6.2. Effect of unresolved stress models

We consider three different unresolved stress models, namely constant eddy-viscosity (SC), dynamic Smagorinsky (DS) and dynamic one-coefficient mixed (DM). In SC, we simply replace ν in (4.10) and (4.11) by $(1 + e)\nu$. Notice that the mean velocity equation is unchanged, meaning that there is no, or only a weak, interaction with the unresolved modes in the equation and in the Reynolds shear stress. The choice of $e = 0.8$ in SC is not the most optimal value; however the model predicts the best wall-normal turbulent intensity among different values of e in our tested simulations. Note that the choice of $e = 0$ produces the best streamwise turbulent intensity among other choices of e . All statistical reconstructions include the unresolved stress contribution whenever possible:

$$\langle \tau_{ij}^{S4/SC} \rangle = \langle u_i < u_{j<} \rangle; \quad \langle \tau_{ij}^{DS} \rangle = \langle u_i < u_{j<} \rangle + \langle \tau_{12>}^{DS} \rangle \delta_{i1} \delta_{j2}; \quad \langle \tau_{ij}^{DM} \rangle = \langle u_i < u_{j<} \rangle + \langle \tau_{ij>}^{DM} \rangle.$$

Figure 8 shows the mean velocity profile from different models and the mean velocity prediction from the law of wall in dashed lines as a function of the wall distance. Every model except SC predicts an accurate mean velocity profile with a good intercept of the log layer, consistent with an accurate prediction of the friction Reynolds number as shown in table 3. Among these models, DM yields the best prediction. The high intercept of the log law in SC suggests a low friction Reynolds

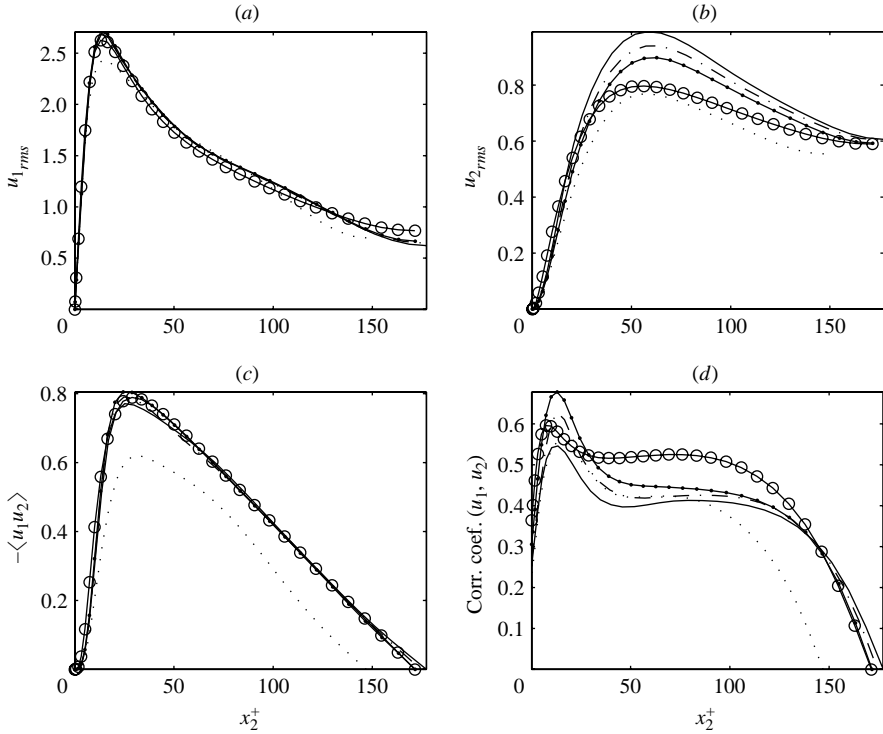


FIGURE 9. Statistics from simulations: (a) streamwise turbulent intensity, (b) wall-normal turbulent intensity, (c) Reynolds shear stress and (d) correlation coefficient of streamwise and wall-normal velocity: solid, S4 (no unresolved stress model); dotted, SC (constant eddy-viscosity); dash-dot, DS (dynamic Smagorinsky model); points, DM (dynamic mixed model); circles, LES.

number. Again, the accuracy of Reynolds shear stress prediction plays an important role in the accuracy of the mean velocity prediction.

Figure 9(a) shows the streamwise turbulent intensity from different models. All the models except SC produce fairly accurate intensity profiles. This suggests the turbulence production mechanism and the distribution of streamwise turbulent intensity are strongly controlled by the shape of PODS eigenfunctions regardless of the choice of unresolved stress models, at least for the 4 PODS family model case. Not only does SC fail to predict the peak of streamwise turbulent intensity, but SC also fails to capture the qualitative shape of the intensity (relatively low intensity in $x_2^+ \leq 40$ and $x_2^+ \geq 100$ regions). The quantitative, dynamical models require more sophisticated unresolved stress models than a uniform eddy-viscosity model (SC).

Figure 9(b) shows the wall-normal turbulent intensity. In this case, SC gives the best estimate of the intensity. However, we have to sacrifice some accuracy of the mean velocity and streamwise turbulent intensity profile. The introduction of the unresolved stress model into the dynamical system (DS, DM) evidently improves the intensity prediction from S4, but still fails to completely remove the anomalous activity in the higher-order resolved eigenmodes in S4. We suspect that the interaction with unresolved modes in the wall-normal direction, which is not accounted for by the dynamic procedure (§4.3), plays an important role in the actual unresolved stresses. We may draw the same conclusion for the spanwise turbulent intensity (see Juttijudata 2003).

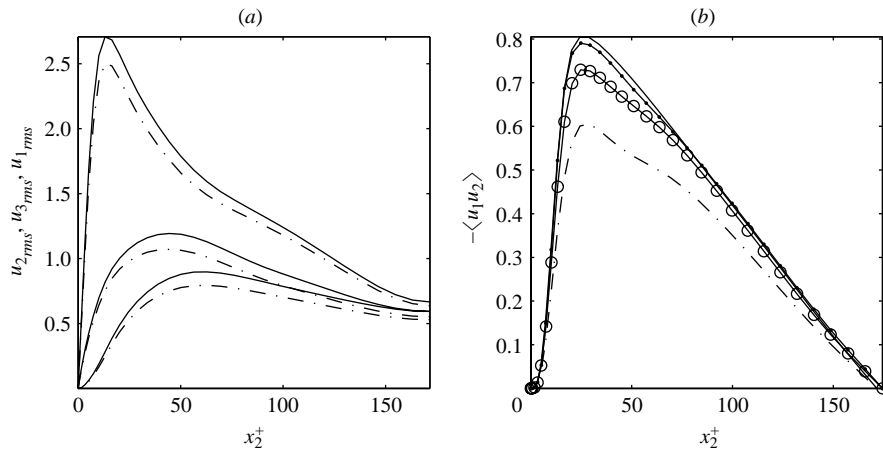


FIGURE 10. Contribution from unresolved stresses: (a) component turbulent intensities; solid, total intensities (DM-dynamic mixed model); dash-dot, resolved intensities (DM-dynamic mixed model), (b) Reynolds shear stress: solid, total RS (DM-dynamic mixed model); dash-dot, resolved RS (DM-dynamic mixed model); circles, total RS (DS-dynamic Smagorinsky model); points, resolved RS (DS-dynamic Smagorinsky model).

Figure 9(c) shows the reconstructed Reynolds shear stress from different models. The Reynolds shear stress predictions from both DS and DM slightly are improved from the prediction from S4. The prediction from SC fails to produce an accurate Reynolds shear stress profile, re-emphasizing the insufficiency of the uniform eddy-viscosity model. Figure 9(d) shows the correlation coefficients as a function of the wall distance. On average, none of the unresolved stress models improves the accuracy of the coefficient prediction compared to the S4 prediction. Since the quality of the prediction of wall-normal turbulent intensity prediction from DS and DM is slightly deteriorated compared to that from S4, DS and DM slightly over-predict the maximum value of the coefficient.

Before closing this section, let us consider the contribution from the unresolved stresses to the total stresses. Figure 10(a) shows the resolved and total (resolved and unresolved) turbulent intensities from DM model. The contribution of the unresolved stress is fairly small compared to the total intensities (less than 10%). Figure 10(b) shows the resolved and total Reynolds shear stress from DS and DM. The contribution of the unresolved stress in DS is fairly small (less than 10%) whereas that in DM is quite considerable (up to 20%). However, the total Reynolds shear stresses from both models are almost the same and insensitive to the unresolved stress models. In fact, they are not much different from the S4 prediction, which has no unresolved stress model. The interaction of resolved, unresolved and mean motion is quite complicated and very sensitive to the details of the unresolved stress model. Further understanding of the nonlinear energy transfer is required. We will leave this issue for future study.

6.3. Statistical structures

In this section, we will examine the structures of turbulent motion from numerical simulations. We will present the structures from DM only. The other models produce qualitatively similar structures. Let us consider the two-point correlations in the spanwise direction at $x_2^+ = 13$. The mean streak spacing may be estimated by doubling the separation of the minimum correlation of the streamwise velocity, R_{11} , shown in figure 11. With $\Delta x_3^+ \approx 50$ from the figure, the mean streak spacing is approximately

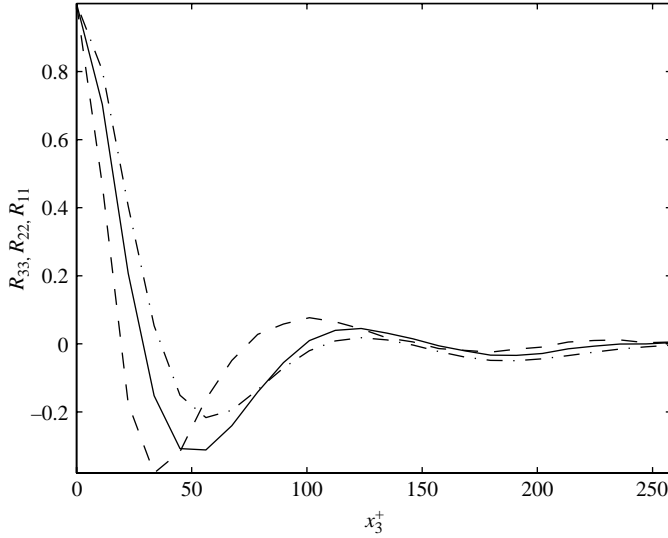


FIGURE 11. Spanwise two-point correlations at $x_2^+ = 13$: solid, R_{11} ; dashed, R_{22} ; dot-dash, R_{33} .

$100 \nu/u_\tau$, consistent with the visual observation in Robinson (1991). The diameter of the streamwise vortices may be approximated by the separation of the minimum correlation of the wall-normal velocity, R_{22} , shown in figure 11. The estimate of R_{22} suggests a diameter of the vortices of about $40 \nu/u_\tau$, also consistent with the observation in Robinson (1991). We find the separation of the minimum correlation of spanwise velocity, R_{33} , shown in the same figure, to be about $50\text{--}60 \nu/u_\tau$. This could suggest the presence of counter-rotating vortex pairs in the wall region. However as we further move toward the centre of the channel, we no longer find the minimum point of the correlation above $x_2^+ > 30$ (not shown). The minimum correlation coefficient we observed at $x_2^+ = 13$ might be due to the impingement or splatting effect caused by a single vortex as suggested by Moser & Moin (1984).

Figure 12 shows the instantaneous velocity reconstruction at $x_2^+ = 13$. Part (a) of the figure shows the fluctuating streamwise velocity contours (dashed line represents low speed; solid line represents high speed), and part (b) shows the ejections (solid line) and sweeps (dashed line). Low-speed streaks are relatively long and thin compared to high-speed streaks. From visual inspection, low-speed streak spacing is around $100 \nu/u_\tau$. We also find a high degree of coherence between low-speed streaks and ejections as well as high-speed streaks and sweeps: low-speed (high-speed) streaks more or less sit on top of ejections (sweeps).

The fluctuating velocity reconstruction at the $x_1^+ = 0$ cross-section of the same case is reproduced in figure 13. Part (a) of the figure shows the streamwise velocity contours, and part (b) shows the velocity vectors of the spanwise and wall-normal components. They show alternating regions of low-speed and high-speed streaks especially above and below $x_2^+ = 100, -100$. There is also evidence of vortical structures. A strong correlation of low-speed (high-speed) regions and ejections (sweeps) also appears e.g. at $x_2^+ = -125$ (-90) and $x_3^+ = 275$ (220). Figure 14 shows the fluctuating velocity field of the streamwise-invariant modes in figure 13. The streamwise velocity contours and velocity vectors are much more coherent than in figure 13. The presence of streaks and vortical structures is also much more clear in this figure.

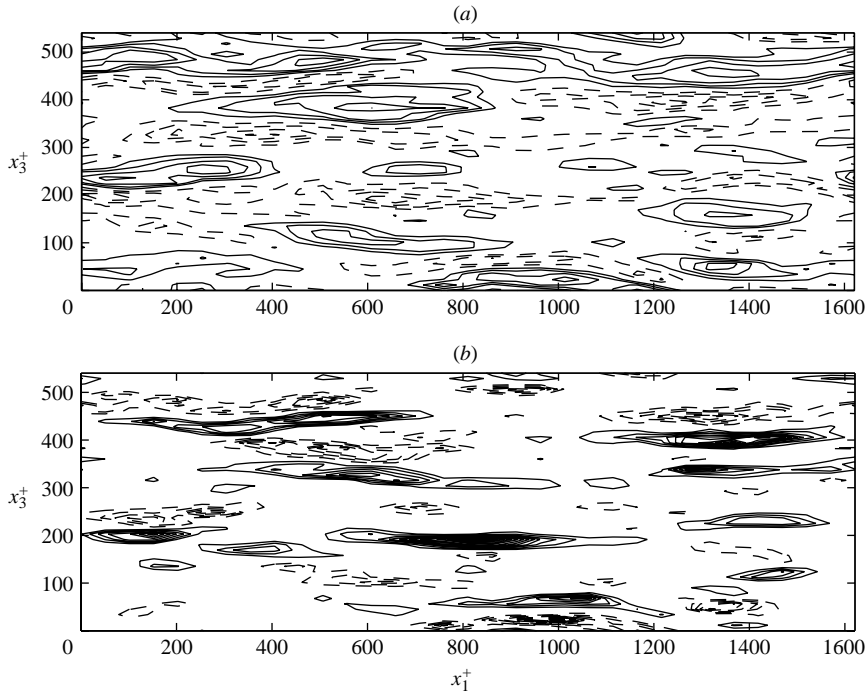


FIGURE 12. The instantaneous velocity reconstruction from DM projected on $x_2^+ = 13$ plane. (a) Contours of streamwise velocity: solid, high-speed; dashed, low-speed; (b) contours of ejections and sweeps; solid, ejections; dashed, sweeps.

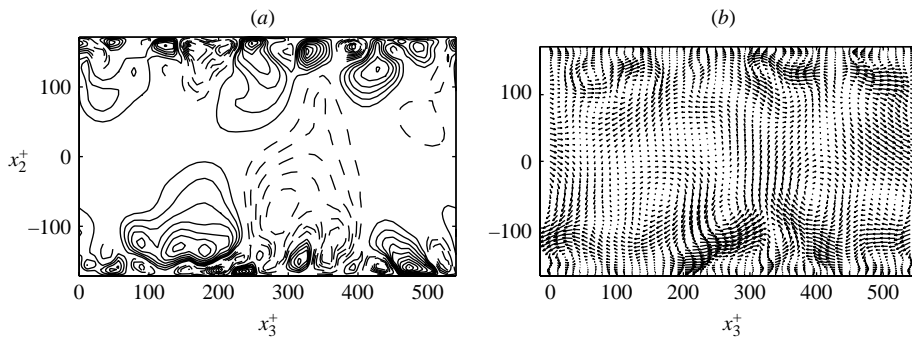


FIGURE 13. The instantaneous velocity reconstruction from DM projected on $x_1^+ = 0$ plane. (a) Contours of streamwise velocity: solid, high-speed; dashed, low-speed, (b) velocity vectors of spanwise and wall-normal velocity.

7. Conclusion

Our main objective in this study is to develop new POD basis functions and their dynamical models to achieve better accuracy. Re-examination of the POD statistical reconstruction and its structures suggest that the resulting coherent structures are too well correlated due to the relatively slow convergence rate of the wall-normal velocity component and the overproduction of the Reynolds shear stress in low-order POD modes. A close examination reveals that the too-coherent structures of the POD expansion have resulted from the directional preference of the low-order

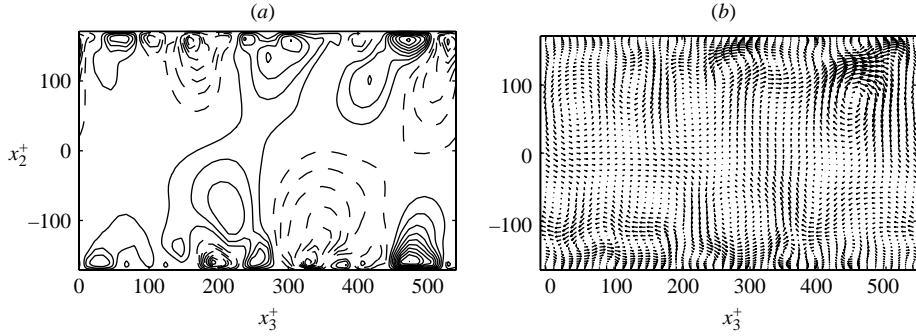


FIGURE 14. The instantaneous velocity reconstruction from streamwise-invariant modes of DM projected on $x_1^+ = 0$ plane. (a) Contours of streamwise velocity: solid, high-speed; dashed, low-speed, (b) velocity vectors of spanwise and wall-normal velocity.

eigenfunctions toward the most energetic data points, which are the streamwise motion at the maximum production ($x_2^+ = 13$). Better basis function can be obtained by means of the POD in Squire's coordinate system (PODS). The Squire transformation can approximately confine the streaks to the minus-modes and streamwise vortices to the plus-modes; hence it approximately isolates the more energetic streamwise component from the lateral components. The statistics and structures of the PODS reconstruction improve significantly that of the POD reconstruction. The PODS eigenvalues of the full channel domain suggest that the length scales of the coherent structures are approximately $1650 \nu/u_\tau$ in the streamwise direction and $275 \nu/u_\tau$ in the spanwise direction, which are comparable to the length scales found in physical structures of turbulent boundary layers.

We have developed dynamical models based on PODS. Clearly, the PODS-based model (S4) without any unresolved stress model performs much better than the POD-based models (P6 and P8). It performs particularly well in capturing mean velocity, streamwise turbulent intensity and Reynolds shear stress, and compares favourably to POD models that have the same energy content (P6), or require comparable computational effort (P8). The effect of unresolved stress models on the dynamical model is also considered. It is evident that a constant eddy-viscosity model (SC) is not sufficient to model the interaction with the unresolved motion in the quantitatively accurate models. In general, the dynamic Smagorinsky (DS) and one-coefficient mixed unresolved stress models (DM) produce comparably accurate statistics and are only slightly better than the dynamical model without any unresolved stress model. The comparison of the total stresses to the resolved stresses in DS and DM suggests that the resolved stresses strongly depend on the unresolved model but the total stresses are not much different from one another, including the model without any unresolved stress model. The reconstruction of the spatial structures of PODS simulation suggests the presence of streaks, streamwise vortices and the ejection/sweep events which resemble the spatial structures in turbulent boundary layers.

It is also important to consider the increased computational resources required by the PODS models. Table 4 shows the CPU time per δ/U_c normalized by the CPU time of the S4 model. The numbers reported in the table can only suggest the qualitative trends of each model because they strongly depend on the implementation and machine. Even though P6 saves 10 % compared to S4, S4 produces a much more accurate result than P6. The costs of solving S4, DS and DM are not much different.

Case	CPU Time
P6	0.91
P8	1.09
S4	1.00
SC	0.72
DS	1.04
DM	0.98
LES	1.14
CDNS	0.46

TABLE 4. Relative CPU time per δ/U_c .

P8 and LES require about 10–15 % more computational time than S4, DS and DM. In terms of the solution accuracy and computational cost, LES still does have advantages over other models. The relatively large CPU time required by P8 is due to a stronger velocity gradient at the wall which decreases the maximum allowable time step, and the relatively small CPU time required by SC is due to a milder velocity gradient at the wall which increases the maximum allowable time step.

Better understanding of the dynamics of coherent structures from a PODS viewpoint, the nonlinear interaction of PODS models, and the development of new closure models and boundary condition models for the localized domain models are recommended for future study.

This research was conducted using the resources of the Cornell Theory Center, which receives funding from Cornell University, New York State, federal agencies, foundations, and corporate partners. The computational time at the Cornell Theory Center was also partially supported by the National Science Foundation, Grant No. CTS-0106064. V.J. gratefully acknowledged the financial support from the Royal Thai Government.

REFERENCES

- AUBRY, N., HOLMES, P., LUMLEY, J. L. & STONE, E. 1988 The dynamics of coherent structures in the wall region of a turbulent boundary layer. *J. Fluid Mech.* **192**, 115–173.
- BAKEWELL, H. P. & LUMLEY, J. L. 1967 Viscous sublayer and adjacent wall region in turbulent pipe flow. *Phys. Fluids* **10**, 1880–1889.
- BALL, K. S., SIROVICH, L. & KEEFE, L. R. 1991 Dynamical eigenfunction decomposition of turbulent channel flow. *Intl J. Numer. Meth. Fluids* **12**, 585–604.
- BARDINA, J., FERZIGER, J. & REYNOLDS, W. 1983 Improved turbulence models based on large eddy simulation of homogeneous, incompressible, turbulent flows. *Tech. Rep.* TF-19. Thermosciences Division, Mechanical Engineering Department, Stanford University.
- BERKOOZ, G., HOLMES, P. & LUMLEY, J. L. 1991 Intermittent dynamics in simple models of the wall layer. *J. Fluid Mech.* **230**, 75–95.
- BERKOOZ, G., HOLMES, P. & LUMLEY, J. L. 1993 The proper orthogonal decomposition in the analysis of turbulent flows. *Annu. Rev. Fluid Mech.* **25**, 539–575.
- BERKOOZ, G., HOLMES, P., LUMLEY, J. L., AUBRY, N. & STONE, E. 1994 Observations regarding “Coherence and chaos in a model of turbulent boundary layer” by X. Zhou and L. Sirovich. *Phys. Fluids* **6**, 1574–1578.
- CANUTO, C., HUSSAINI, M. Y., QUATERONI, A. & ZANG, T. A. 1988 *Spectral Methods in Fluid Dynamics*. Springer.
- CORINO, E. R. & BRODKEY, R. S. 1969 A visual investigation of the wall region in turbulent flow. *J. Fluid Mech.* **37**, 1–30.

- DEAN, R. B. 1978 Reynolds number dependence on skin friction and other bulk flow variables in two-dimensional rectangular duct flow. *Trans. ASME I: J. Fluids Engng* **100**, 215–223.
- GIBSON, J. F. 2002 Dynamical systems models of wall-bounded shear-flow turbulence. PhD thesis, Cornell University.
- HEISENBERG, W. 1948 On the theory of statistical and isotropic turbulence. *Proc. R. Soc. Lond. A* **195**, 402–406.
- HERZOG, S. 1986 The large scale structures in the near-wall region of turbulent pipe flow. PhD thesis, Cornell University.
- HOLMES, P., LUMLEY, J. L. & BERKOOZ, G. 1996 *Turbulence, Coherent Structures, Dynamical Systems and Symmetry*. Cambridge University Press.
- JUTTIJUDATA, V. 2003 Proper orthogonal decomposition in Squire's coordinate system and its low-dimensional model of channel turbulence. PhD thesis, Cornell University.
- JUTTIJUDATA, V., REMPFER, D. & LUMLEY, J. L. 2001 Development of near-wall SGS model based on a localized low-dimensional approach. *Bull. APS* **46**, No. 9.
- KIM, J., MOIN, P. & MOSER, R. D. 1987 Turbulence statistics in fully-developed channel flow at low Reynolds number. *J. Fluid Mech.* **177**, 133–166.
- KLINE, S. J., REYNOLDS, W. C., SCHRAUB, F. A. & RUNSTADLER, P. W. 1967 The structure of turbulent boundary layers. *J. Fluid Mech.* **30**, 741–773.
- LEONARD, A. & WRAY, A. A. 1982 A new numerical method for the simulation of three-dimensional flow in a pipe. In *Eighth Intl Conf. on Numerical Methods in Fluid Dynamics* (ed. E. Krause), pp. 335–342. Springer.
- LOÈVE, M. 1955 *Probability Theory*. Van Nostrand.
- LUMLEY, J. L. 1967 The structure of inhomogeneous turbulence. In *Atmospheric Turbulence and Wave Propagation* (ed. A. M. Yaglom & V. I. Tatarski), pp. 166–178. Nauka, Moscow.
- LUND, T. S. 1998 On the use of discrete filters for large-eddy simulation. In *Center for Turbulence Research Annual Briefs 1997*, p. 83. Stanford University, Stanford.
- MA, X. & KARDIANAKIS, G. K. 2002 A low-dimensional model for simulating three-dimensional cylinder flow. *J. Fluid Mech.* **458**, 181–190.
- MOIN, P. & MOSER, R. D. 1989 Characteristic-eddy decomposition of turbulence in a channel. *J. Fluid Mech.* **200**, 471–509.
- MOSER, R. D. & MOIN, P. 1984 Direct numerical simulation of curved channel turbulent channel flow. *Tech. Rep. NASA TM-85974*. NASA.
- MOSER, R. D., MOIN, P. & LEONARD, A. 1983 A spectral numerical method for the Navier–Stokes equations with application to Taylor–Couette flow. *J. Comput. Phys.* **52**, 524–544.
- OMURTAG, A. & SIROVICH, L. 1999 On low-dimensional modeling of channel turbulence. *Theoret. Comput. Fluid Dyn.* **13**, 115–127.
- PODVIN, B. 2001 On the adequacy of the ten-dimensional model for the wall layer. *Phys. Fluids* **13**, 210–224.
- PODVIN, B. & LUMLEY, J. L. 1998 A low-dimensional approach for the minimal flow unit. *J. Fluid Mech.* **362**, 121–155.
- REMPFER, D. 1993 Low-dimensional models of a flat plat boundary layer. In *Proc. Near-Wall Turbulent Flows* (ed. R. M. C. So, C. G. Speziale & B. E. Launder), pp. 63–72. Elsevier.
- ROBINSON, S. K. 1991 Coherent motions in the turbulent boundary layer. *Annu. Rev. Fluid Mech.* **23**, 601–639.
- SARGHINI, F., PIOMELLI, U. & BALARAS, E. 1999 Scale-similar models for large-eddy simulations. *Phys. Fluids* **11**, 1596–1607.
- SIROVICH, L. 1987 Turbulence and the dynamics of coherent structures, Parts I–III. *Q. Appl. Maths* **XLV**, 561–590.
- SIROVICH, L., BALL, K. S. & HANDLER, R. A. 1991 Propagating structures in wall-bounded turbulent flows. *Theoret. Comput. Fluid Dyn.* **2**, 307–317.
- SIROVICH, L., BALL, K. S. & KEEFE, L. R. 1990 Plane waves and structures in turbulent channel flow. *Phys. Fluids A* **2**, 2217–2226.
- SIROVICH, L. & ZHOU, X. 1994 Reply to “observations regarding ‘Coherence and chaos in a model of turbulent boundary layer’ by X. Zhou and L. Sirovich”. *Phys. Fluids* **6**, 1579–1582.
- SMAGORINSKY, J. 1963 General circulation experiments with the primitive equations: I. the basic equations. *Mon. Weath. Rev.* **91**, 99–164.

- SPALART, P. R., MOSER, R. D. & ROGER, M. M. 1991 Spectral methods for the Navier–Stokes equations with one infinite and two periodic directions. *J. Comput. Phys.* **96**, 297–324.
- SQUIRE, H. B. 1933 On the stability for three-dimensional disturbances of viscous fluid flow between parallel walls. *Proc. R. Soc. Lond. A* **142**, 621–628.
- STUART, J. T. 1963 Hydrodynamic stability. In *Laminar Boundary Layers*, Chap. 9 (ed. L. Rosenhead), pp. 492–579. Oxford University Press.
- TENNEKES, H. & LUMLEY, J. L. 1972 *A First Course in Turbulence*. MIT Press.
- WALEFFE, F. 1995 Transition in shear flows. nonlinear normality versus non-normal linearity. *Phys. Fluids* **7**, 3060–66.
- ZHOU, X. & SIROVICH, L. 1992 Coherence and chaos in a model of turbulent boundary layer. *Phys. Fluids A* **4**, 2855–2874.